ACS Catalysis

pubs.acs.org/acscatalysis Review

Photocatalytic CO_2 Reduction: A Review of Ab Initio Mechanism, Kinetics, and Multiscale Modeling Simulations

Žan Kovačič, Blaž Likozar,* and Matej Huš*

Cite This: *ACS Catal.* 2020, 10, 14984–15007 Read Online

ACCESS | Metrics & More | Article Recommendations

ABSTRACT: Climate change has prompted scientists to search for possible ways of reducing CO_2 emissions or even capturing it from the atmosphere. Catalytic reduction of CO_2 into value-added chemicals has been put forward as a viable strategy. While thermocatalytic routes of producing CO, methanol, methane, and higher hydrocarbons from CO_2 have been the focus of considerable research efforts, photocatalytic conversion is an emerging approach. Photoactivation of CO_2 has potential as a greener process because it could be carried out at lower temperatures and pressures, decreasing the energy consumption. The recent advent of available computational power and tools has made it possible to study the reaction in silico for catalyst prediction and mechanism elucidation. In this Review, we thus focus on ab initio research of photocatalytic CO_2 reduction and comparison with experiments. The most commonly used materials are variously doped TiO_2, g-C_3N_4, and perovskites, which have favorable optical properties on their own. Their efficiency is mostly governed by the band gap, charge separation, and charge transfer. Their characteristics can be improved, and the catalysts can be tailored for a specific use by doping, introduction of defects (such as oxygen vacancies or geometric effects), cocatalysts, or using Z-scheme catalysts. Most theoretical studies focus on the calculations of conduction and valence bands, band gap, and adsorption energies. Some studies try to describe the reaction mechanism. Few studies go beyond the hybrid-functional DFT approach and try to explicitly model the effect of electron excitation. While a theoretical description of the excited states is possible with post-DFT methods, it has yet to be applied to the problem of CO_2 photoreduction on a larger scale. We conclude the Review with an outlook on how the current state-of-the-art can be used for improving the existing catalysts.

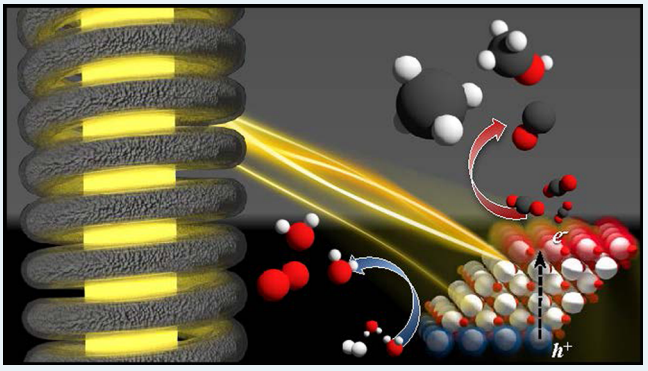

KEYWORDS: *photocatalysis, CO_2, reduction, theoretical modeling, multiscale*

1. INTRODUCTION

After industrialization and becoming a carbon-based society, rising CO_2 emissions have become a serious environmental problem because of its implications in climate change. The most straightforward way of tackling this problem is to reduce the emissions, but this might not be enough or even possible in all instances, where the use of fossil fuels cannot be simply avoided. A more proactive approach is to capture and convert CO_2 into value-added products.[1] Unsurprisingly, the conversion of CO_2 has received significant research attention in recent years because of the many challenges faced. CO_2 is a very stable and inert compound on account of a high C═O bond energy (750 kJ mol^{-1}),[2] requiring high temperatures and pressures for thermocatalytic conversion. A different viable approach is to convert CO_2 using light (photocatalysis) or electricity (electrocatalysis).

The redox potential for a single electron transfer to CO_2 is −1.85 eV (vs NHE at pH = 7). This high value stems from the fact that bending a linear CO_2 molecule and injecting an electron into its orbitals is unfavorable. The redox potential is lower than the conduction band (CB) of most semiconductors.[3,4]

$$CO_2 + e^- \rightarrow CO_2^- \qquad E^\circ = 1.85\ \text{V} \tag{1}$$

However, on certain photocatalysts, CO_2 can bind in a bent configuration. An electron transfer from CO_2 upon photoexcitation to form the CO_2^- anion is therefore an essential process, which is dependent on the geometry of the adsorbed CO_2.[5,6] In a bent configuration, CO_2 exhibits a lower LUMO

Received: June 10, 2020
Revised: November 25, 2020
Published: December 7, 2020

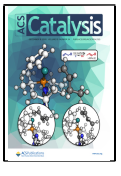

https://dx.doi.org/10.1021/acscatal.0c02557
ACS Catal. 2020, 10, 14984–15007

level, which in turn facilitates the electron transfer. This means that in order to more easily reduce CO_2, adsorption in a bent configuration makes it more susceptible to receiving an electron. While a thermocatalytic CO_2 reduction requires high temperatures (at least 500 K) and pressures (10 bar),[7] photocatalysis can take place at room temperature and ambient pressure, with (sun)light providing the required excitation energy. As a consequence, many semiconductors have been studied for their photocatalytic properties. Upon reduction, different products might form. On copper, hydrocarbons are preferred,[8] while silver favors CO.[9,10] In liquid systems, HCOOH and CH_3OH are also often formed.

The most studied materials for the photoreduction of CO_2 are metal oxides, particularly, TiO_2,[11−13] MgO,[14,15] Ga_2O_3,[16] Bi_2MoO_6,[17] In_2O_3,[18] and Ta_2O_5.[19] Often, these materials are further (surface-)doped with metals such as Pt, Cu, Cr, Ru, Pd, Ag, Fe, Co, and Ni,[20−22] which diminish the charge recombination. This happens because of the metal acting as an electron sink, effectively trapping the electrons and stabilizing charge separation, thus improving the photocatalytic properties of the material.[23,24]

Another technique besides doping is to combine different materials to improve their properties: such as the band gap, electron densities, and stability. Combined photocatalysts such as $CdSe/Pt/TiO_2$,[25] CeO_2/Bi_2MoO_6,[26] $Ag/MgO/TiO_2$,[27] and CeO_x-$S/ZnIn_2S_4$[28] have been extensively studied. In recent years, there has also been a growing interest in metal-free catalysts. Special attention has been devoted to g-C_3N_4 because of its nontoxicity, good stability, good absorption in the visible spectrum, and a low band gap of 2.7 eV.[29] Despite these qualities, charge recombination hinders its photocatalytic activity.[30] There have been several solutions proposed, such as doping (for instance with S[31], N[32], Nb, Ta, N, C[33]) or using cocatalysts deposited on the catalytic surface and acting as electron traps.[23] Cocatalysts are usually metals, such as Pd,[34] Au,[35,36] Ag,[37,24] Pt,[38] Cu,[20] Fe, Co, Ni.[21] Note that surface doping or using cocatalysts differs from traditional bulk doping.

A promising alternative to cocatalysts are the so-called Z-scheme catalysts.[39] It is possible to exploit a high conduction band minimum of one semiconductor and a low valence band maximum of another one. This arrangement is called the Z-scheme and can be direct (semiconductors in contact) or indirect (a medium between the semiconductors enables the electron flow). Within the indirect Z-scheme, spatial separation can prolong the lifetime of the electrons and holes.[40] This avoids the problem of finding *one* material with (1) a sufficient bandgap for the CO_2 reduction, (2) a conduction band negative enough for the reduction of CO_2 to CO_2^- to proceed. Z-scheme catalysts help overcome large overpotentials, increasing their photocatalytic activity.[41,42] There are many reported Z-scheme catalysts, for instance, $Ag_2WO_4/g\text{-}C_3N_4$,[43] $Fe_2V_4O_{13}/RGO/CdS$,[44] $g\text{-}C_3N_4/SnS_2$,[41] $Ag_3PO_4(111)/g\text{-}C_3N_4$,[45] Ag_3PO_4/TiO_2,[46] $Al_2O_3/g\text{-}C_3N_4$.[47] Research mostly focuses on synthesis, characterization, and experimental performance, while the theoretical modeling is scarce.

Another way of improving a material is by introducing defects. Reports on the effects of defects (such as oxygen vacancies on photocatalytic properties of material) are somewhat inconsistent. Some researchers report that vacancies act as a charge recombination centers retarding the photocatalytic activity,[48,49] while others found an increase in the activity.[50,51] Bulk defects act as recombination centers,[52] while defects on surfaces seem to improve photocatalytic activity as oxygen vacancies act as electron traps.[53] Oxygen defects on the surface enhance the photocatalytic activity[17,18,54,55]

Thus, there are several methods for improving photocatalytic properties of a material. The general consensus is that a good photocatalytic material should encompass a good charge separation, a fast charge transfer, absorption in the visible part of the spectrum, high stability, low cost, and nontoxicity.[56,57] Finding a photocatalyst that fulfils all of the above requirements is a remarkably difficult endeavor. Although the trial-and-error approach has historically revealed several well performing catalysts, such as TiO_2, further improvements can be achieved systematically. Computer-based design of the catalyst material is expected to play a crucial role, which underscores the importance of theoretical modeling in understanding the material properties and reaction mechanism.

In this Review, we focus on a theoretical *first-principles* description of CO_2 photoreduction and subsequent kinetic or multiscale modeling based on these results. In Section 2, we discuss the fundamentals of photocatalytic CO_2 reduction. In Section 3, we focus on the theoretical description of this reaction on different scales: the electronic level, kinetic simulations, and macroscale modeling (joining them together is called a multiscale approach). Then in Section 4, an overview of CO_2 adsorption on photoactive materials is presented, followed by the first-principles calculations of materials *properties* (such as band gaps and conducting bands) in Section 5. In Section 6, an overview of the proposed mechanisms is presented together with multiscale modeling endeavors. We conclude with an outlook and future prospects in the last part.

2. FUNDAMENTALS OF PHOTOCATALYTIC CO_2 REDUCTION AND DOPING

While photocatalysis offers an attractive alternative to high temperature and pressure thermocatalytic reactions with the possibility of operating at ambient temperature and pressure, there are still drawbacks such as low yields, poor light absorption,[58] and photocorrosion.[59] Low yields are attributed to high charge recombination,[60,61] inappropriate band gaps,[62] and slow electron transfer, while poor light absorption is caused by wider band gaps and only UV light having the sufficient energy to overcome the forbidden gap.[62] The loss of photocatalytic activity via photocorrosion and the problem of stability is another challenge of photocatalysts.[63]

For any chemical reaction to proceed, the Gibbs (or Helmholtz under constant volume) free energy of the products must be lower than that of the reactants. In other words, the system's free energy must decrease. There are several ways to achieve this: with temperature, reactant/product concentrations, applied electrochemical potential, incident light, and so on. The required reduction potentials (versus the standard hydrogen electrode) for CO_2 reduction are[64,65]

$$CO_2 + 2H^+ + 2e^- \rightarrow HCOOH \qquad E^\circ = -0.66\ V \tag{2}$$

$$CO_2 + 2H^+ + 2e^- \rightarrow CO + H_2O \qquad E^\circ = -0.52\ V \tag{3}$$

$$CO_2 + 4H^+ + 4e^- \rightarrow CH_2O + H_2O \qquad E^\circ = -0.49\ V \tag{4}$$

https://dx.doi.org/10.1021/acscatal.0c02557
ACS Catal. 2020, 10, 14984−15007

$$CO_2 + 6H^+ + 6e^- \rightarrow CH_3OH + H_2O \qquad E^\circ = -0.40\ V \tag{5}$$

$$CO_2 + 8H^+ + 8e^- \rightarrow CH_4 + 2H_2O \qquad E^\circ = -0.25\ V \tag{6}$$

In photocatalysis, the conduction band minimum of the material determines the energy of the photoexcited electrons and must be lower than the reduction potential for the given reaction in order for it to occur.[66] Semiconductors are most suitable for this because they exhibit a measurable yet surmountable energy difference between the highest (occupied) valence band and lowest (unoccupied) conduction band, partially conducting even without photoexcitation because of the Boltzmann tail. In metals, there is no ("forbidden") gap between the valence band maxima (VBM) and conduction band minima (CBM), enabling the electrons to move freely. Insulators, on the other hand, exhibit a prohibitively large band gap. Semiconductors (depending on the semiconductor) lie somewhere in-between. The chemical potential of electrons in a semiconductor (or any material, for that matter) is defined analogously as that of any other species. It is the change in free energy when the species (electron) are added or removed from an (infinitely large) system. A related quantity is the Fermi level (E_F), which is defined as the work required for the addition of one electron.

Upon irradiation, electrons from VBM are excited to CBM, leaving vacancies ("holes") in the valence band. The electrons and holes that do not recombine and reach the interface can partake in a photocatalyzed reaction. For a more in-depth theoretical discussion, the reader is referred to the review by Xu and Carter.[64]

Conceptually, photocatalysis occurs in three steps,[67] as depicted in Figure 1. In the first step, a photon is absorbed,

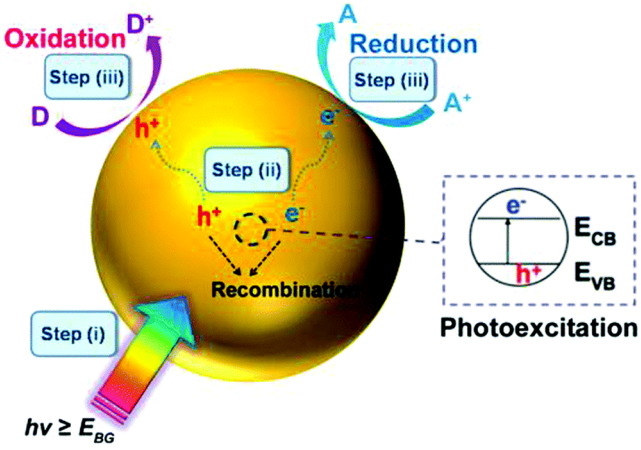

Figure 1. Three-step process in photocatalysis: (i) photoexcitation, (ii) charge separation, and (iii) charge transfer with the corresponding oxidation/reduction reactions. Reprinted with permission from ref 67. Copyright 2016 Royal Society of Chemistry.

exciting an electron from the valence band to the conduction band and leaving a hole (vacancy) in the valence band. These electron–hole pairs can either recombine in the bulk or diffuse toward the surface, which brings about the second step, consisting of charge separation and diffusion to the surface. In the third step, the electrons and holes at the interface partake in the reduction and oxidation reactions, respectively. To improve the process, it is imperative that the photocatalyst to a large extent absorb as much light as possible and prevent charge recombination upon excitation. This can be achieved by doping, codoping, deposition of cocatalysts, introducing defects (e.g., oxygen vacancies), or combining different semiconductors (e.g., Z-scheme).

It is crucial that the lifetime of photoexcited electrons be long enough, which is mostly governed by the electron–hole recombination rate. This lifetime can be prolonged by trapping the electrons in a state of different multiplicity (singlet/triplet), making their recombination a spin-forbidden event. During the conversion of the singlet photoexcited state to the triplet photoexcited state, energy loss should be minimal to improve quantum efficiency. Doping can help with compound semiconductors if excited electrons and holes are physically located on different atoms, minimizing the exchange splitting. Transition metals with empty, full, or half-full d-orbitals have particularly stable electron configurations and might prove beneficial in doping as they are less likely to trap electrons.[68]

A crucial characteristic of all semiconductors is the band gap. The band gap represents the energy needed to excite an electron from the valence band (VB) to the conduction band (CB). The band gap is intimately connected to the wavelength of the incident light to which the photocatalytic material is most responsive. However, the value of the band gap has also other consequences. For instance, according to the ultimate efficiency hypothesis, a band gap of 1.1 eV is optimal for solar cell applications.[69]

In transition metal-oxide photocatalysts, the 2p orbitals of oxygen mostly contribute to the VBM,[70] located approximately 3 eV above SHE. This is too large for utilizing the wavelengths present in the visible light. As this would require the VBM to be below the reduction potential of CO_2, the VBM can be increased by doping or alloying.

Semiconductors can be doped with elements that introduce excess electron or excess vacancies, resulting in *n*-type or *p*-type materials. In a *n*-type semiconductor, the dopants provide extra electrons, which subsequently introduce the majority carriers, whereas in a *p*-type semiconductor, the same principle applies for holes.[71] Replacing an atom in a semiconductor is therefore considered a defect, which impairs the charge equilibrium. Ghuman et al.[72] analyzed the doping effect on amorphous TiO_2. They doped TiO_2 with both *n* and *p*-type atoms (Nb and N, respectively) and showed that doping with one type of atoms is beneficial for the reduction of the band gap and the formation of mid gap states. However, these mid gap states acted as recombination centers and hindered the photocatalytic activity. Co-doping with both types of atoms appeared to improve the photocatalytic activity relative to pristine and monodoped TiO_2. This was attributed to the localized charge deep in the band gap for monodoped systems, while in the codoped system the mid gap states were closer to VB and CB, making electrons and holes delocalized and preventing charge recombination. Ma et al. had previously arrived at similar conclusions[33] when examining the codoping effects on anatase TiO_2. By varying the ratio of cation and anion mixing, they showed that codoping prevents recombination without affecting the CBM. Photoabsorption in the visible region was also improved. Li et al.[32] also reported that doping of TiO_2 with N improved not only its photocatalytic properties but also the absorption of the visible light.

An alternative to bulk doping is surface doping (cocatalysts). Li et al.[32] analyzed mesoporous TiO_2 loaded with noble metals (Pt, Au, Ag) for the photocatalytic reduction of CO_2 to

https://dx.doi.org/10.1021/acscatal.0c02557
ACS Catal. 2020, 10, 14984−15007

methane. The dopants played a crucial role as the reaction rates on pristine TiO_2 were negligible, while the Pt-doped catalyst performed best, followed by Au and Ag, demonstrating that cocatalysts promote photocatalytic activity. The effect is a function of the cocatalyst concentration as too much will depress the activity. Surface doping in reasonable amounts can increase the absorption of visible light and prevent the charge recombination as these metals act as electron sinks (Figure 2),[37,73−75] whereas the overabundance of surface dopants can reduce the amount of the light absorbed, thus hindering the activity.

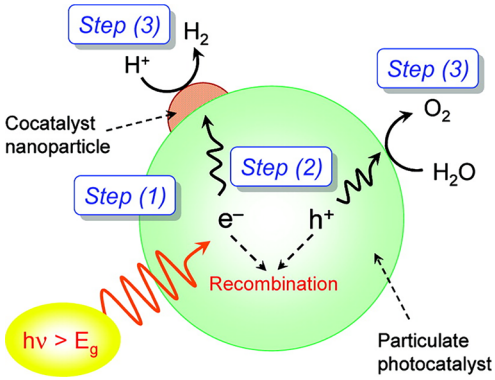

Figure 2. Photocatalysis using a cocatalyst acting as an electron sink on the surface. Reprinted with permission from ref 75. Copyright 2007 American Chemical Society.

Photocatalytic activity can be further tuned by controlling the particle size. Subramanian et al.[35] reported that the Au nanoparticle size affected the photocatalytic reduction efficiency and improved the generation of photocurrent. Jia et al.[23] reported that the nanoparticle size affects not only the overall activity but also the selectivity toward methane. The size of nanoparticles is crucial, as too small particles prevent the electron transfer from the semiconductor to the nanoparticle and excessively large particles act as recombination centers.[76]

The crystallinity of a semiconductor also plays a role because it increases the mobility of electron−hole pairs.[77,78] Therefore, crystalline compounds are preferred over amorphous ones, although for instance, amorphous TiO_2 can be made nearly as active as the crystalline one.[72] Amorphous TiO_2 has a larger surface area, is easier to prepare, and is isotropic. In crystalline materials, not all surfaces exhibit the same photocatalytic activity.[34,23,79] This was elucidated by Cao et al.[34] who studied Pd (111) and Pd (100) nanoparticles on the g-C_3N_4 surface. It was evident that Pd (111) was the preferred surface because Pd (111) is a better electron sink with a better CO_2 adsorption and CH_3OH desorption, shifting the selectivity toward methanol. This difference in activity is brought about by the charge transfer dynamics and strength of adsorption interactions. Similarly Butburee et al.[80] studied how different TiO_2 crystal facets affect CO_2 photoreduction. Investigating three surfaces with different ratios of the (001), (101), and (010) facets, they found the pristine (001) facets to perform the worst. The (010) facet exhibited a 4-fold increase in selectivity toward methane, whereas the coexposure of the (010) and (001) facets resulted in highest yields, which had been observed before.[12] Morphology of a photocatalyst is therefore crucial. Controlling the exposed crystal facets has a significant impact not only on the activity but also on the selectivity.

Photocatalysts encompassing a higher fraction of undercoordinated surface atoms (usually facets with high Miller indices) generally exhibit better catalytic activity. However, these facets are usually thermodynamically less stable than their lower-index counterparts, rendering such finetuning challenging. Nevertheless, a significant progress has been made in recent years in the synthesis of such materials, which was for instance reviewed by Kou et al.[81] and Tu et al.[82]

Finding an ideal photocatalyst is therefore an arduous task. Its photocatalytic activity is affected by the chosen semiconductor, where a wide range of possibilities exist, ranging from metalloids, metal oxides to nonmetal semiconductors and all possible combinations thereof. Additional tuning can be made by doping, deposition of cocatalysts, and Z-scheme structures. Particle size, crystallinity, and even the exposed facets also play a role. Theoretical investigations, such as screening of possible (ideal) photocatalysts, allow us to rule out nonpromising candidates before resorting to experiments.

3. THEORETICAL DESCRIPTION

3.1. Electronic Calculations. Density functional theory (DFT) is the most commonly used approach for quantum calculations because of its favorable cost/performance ratio. Hohenberg and Kohn formulated the two theorems, which underpin the DFT, in 1964.[83] First, for each external potential there exists exactly one ground-state electron density. Second, the density with the lowest total energy is the true density. For DFT to be practically useful, the exchange-correlation functional (XC), stemming from mapping a system of interacting electrons to a system of noninteracting electrons, must be selected wisely.[84]

Historically, a local density approximation (LDA)[85] or general gradient approximation (GGA)[86] was used for XC. In LDA, the exchange-correlation part of the functional depends on the electronic density at the point in space, which brought about significant drawbacks. In GGA, the exchange-correlation part included *also* the derivative of the electronic density, bringing about improved total energies,[86] atomization energies,[87,88] and energy barriers.[89] LDA in general overbinds atoms in solids, while GGA weakens the binding, providing more accurate cohesive energies.[90]

While LDA performs poorly, GGA is still useful for metallic systems. Both approaches suffer from the self-interaction error (a small amount of the interaction of an electron with itself is retained).[91] An important source of incorrect electronic density predictions is the delocalization error of functionals, which tend to spread out the electron density artificially.[92] Cohen et al.[93] discussed this problem on H_2^+ and showed that this error manifests in the underestimation of barriers, band gaps, dissociating energies of molecular ions, and charge transfer excitation energies and overestimation of binding energies of charge transfer complexes and the response to electric fields. Sánchez et al.[94] also attribute these incorrect predictions to the localization and delocalization error. The idea of the delocalization energy is connected to the many-electron self-interaction error.[91] Thus, the electronic structure is described poorly. For instance, these functionals fail to accurately predict the band gap, underestimating it in the range of 30−100%.[95] As they often overstabilize the metallic ground states, the metallicity of the system can be completely off in the most extreme cases. For instance, the antiferromagnetic

https://dx.doi.org/10.1021/acscatal.0c02557
ACS Catal. 2020, 10, 14984−15007

Table 1. A Review of Calculated Band Gap Values for Most Promising Photocatalysts and Comparison with Experimental Values

catalyst	functional	theoretical band gap [eV]	experimental band gap [eV]	references
TiO_2 rutile	PBE-GGA	1.782	3.03	72
	DFT+*U*	2.2		
TiO_2 anatase	PBE-GGA	2.532	3.20	
	DFT+*U*	2.5		
TiO_2 amorphous	PBE-GGA	2.1	3.40	
	DFT+*U*	2.5		
TiO_2 anatase	PBE-GGA	2.00	3.20	141
	PBE-GGA+*U*	3.08		
N-doped TiO_2		2.77		
Fe-doped TiO_2		2.76		
N,Fe-codoped TiO_2		2.73		
TiO_2 rutile	PBE-GGA	1.77	3.1	142
	HSE06	3.05		
anatase TiO_2 (101)	HSE	3.05		143
Pt/TiO_2		3.06		
Pd/TiO_2		3.05		
Rh/TiO_2		2.80		
Ru/TiO_2		3.10		
$GaP(100)/TiO_2(001)$	HSE06 (PBE-GGA)	1.50		128
$Ag_3PO_4(111)/g\text{-}C_3N_4$	PBE0	2.52		45
Ag_3PO_4		2.47		
$Ag_3PO_4(111)$		2.75		
$g\text{-}C_3N_4$	HSE06	2.75		
$g\text{-}C_3N_4$ monolayer		3.13		
$g\text{-}C_3N_4$	HSE06	2.98	2.70	38
$Pd/g\text{-}C_3N_4$		0.64		
$Pt/g\text{-}C_3N_4$		0.72		
$g\text{-}C_3N_4$	HSE06		2.74	126
$1\%KBH\text{-}C_3N_4$			2.66	
$2\%KBH\text{-}C_3N_4$			2.55	
$3\%KBH\text{-}C_3N_4$			2.35	
$5\%KBH\text{-}C_3N_4$			1.74	
$S\text{-}g\text{-}C_3N_4$	PBE-GGA	1.18	2.55	31
$S\text{-}g\text{-}C_3N_4$	HSE06	2.42	2.55	129
$g\text{-}C_3N_4$		2.80	2.70	
$g\text{-}C_3N_4$ monolayer	HSE06	2.76	2.7	144
CdS		2.36	2.4	
CdS(110)		2.36		
$g\text{-}C_3N_4/CdS(110)$		2.02		
B_4C_3 monolayer	HSE06	2.39		127
Zn_2GeO_4	PW91-GGA	2	4.50	124
ZnS wurtzite	PW91-GGA	2.09	3.6−3.8	145
ZnS sphalerite		2.08		
ZnS wurtzite (S-vacancy)		1.30		
ZnS sphalerite (S-vacancy		1.72		
ZnO	PBE-GGA	0.73	3.2	146
N-doped ZnO		0.58		
C-doped ZnO		0.16		
S-doped ZnO		0.55		
ZnS	PBE-GGA	1.92	3.1	147
$Zn_{0.9}Cd_{0.1}S$		1.66	3	
$Zn_{0.7}Cd_{0.3}S$		1.40	2.76	
$Zn_{0.6}Cd_{0.4}S$		1.46	2.57	
$Zn_{0.5}Cd_{0.5}S$		1.36	2.45	
$Zn_{0.4}Cd_{0.6}S$		1.28	2.42	
$Zn_{0.3}Cd_{0.7}S$		1.28	2.35	
$Zn_{0.1}Cd_{0.9}S$		1.18	2.33	
CdS		1.15	2.3	
$ZnSnN_2$ (bulk)	PBE-GGA	0.11		148
$ZnSnN_2$ (monolayer)		0.65		

https://dx.doi.org/10.1021/acscatal.0c02557
ACS Catal. 2020, 10, 14984−15007

Table 1. continued

catalyst	functional	theoretical band gap [eV]	experimental band gap [eV]	references
$ZnSnN_2$ (bilayer)		0.93		
$ZnSnN_2$ (bulk)	PBE0	1.79		
$ZnSnN_2$ (monolayer)		2.39		
$ZnSnN_2$ (bilayer)		2.62		
SiAs (monolayer)	PBE-GGA	1.79		149
GeAs (monolayer)		1.44		
SnAs (monolayer)		1.10		
SiAs (monolayer)	HSE06	2.35		
GeAs (monolayer)		2.08		
SnAs (monolayer)		1.69		
MoS_2 (monolayer)	PBE-GGA	1.25	1.8	150
CdS		2.17	2.42	
MoS_2/CdS		1.02		
MoS_2 (monolayer)	HSE06	1.78	1.8	
CdS		2.41	2.42	
MoS_2/CdS		2.11		
MnO	DFT+*U*/G0W0	4.13	3.90	151
FeO		2.30	2.40	
Fe_2O_3		3.08	2.60	
NiO		3.60	4.00	
Cu_2O		2.17	2.10	
MnO	LDA	0.57	3.5−4.3	152
	PBE	0.93		
	PBE+*U*	1.68		
	HSE	3.82		
	PBE0	4.04		
CeO_2(111)	DFT+*U*	1.99		125
	PBE	2		
BiOBr	PBE-GGA	2.31	2.7	153
Bi_3O_4Br		2.17	2.4	
SnS_2 monolayer	PBE	1.57	2.23	154
	HSE06	2.52		
	G0W0	2.88		

configuration of NiO is an insurmountable problem for a GGA DFT approach.[96] This problem is especially pronounced in metal oxides which represent the majority of semiconductors. However, GGA functionals are still commonly used because of their computational inexpensiveness, making periodic systems of several hundred atoms tractable.

One of the simplest solutions is the introduction of the DFT +*U*[97−99] method, also called the Hubbard model. While plain DFT (LDA, GGA) fails to properly describe the behavior of the transition metals due to a narrow 3d (and higher) band leading to the Coulomb repulsion,[100] the strong on-site Coulomb interaction is described by an additional Hubbard-like term in DFT+*U*. The correction is particularly important for localized d and f electrons.[101] The Hubbard model requires two on-site parameters: *U* (Coulomb) and *J* (exchange), which can be obtained from ab initio calculations (such as solving many-body GW: Green's function),[102,103] which is too expensive for large systems, or, more commonly, determined semiempirically by fitting a particular calculated property (such as band gap, adsorption strength, etc.) to the experimentally known value.

U and *J* parameters are determined semiempirically and have to be fine-tuned *for the quantity* we are interested in and are not transferrable between materials. Even worse, the values of *U* and *J* depend on the environment of each atom, making the method less suitable for systems with considerable spin/oxidation state changes.[104] It is also possible to calculate the parameters consistently from first-principles but that does not offer any improvement to the accuracy of the calculations. Nevertheless, DFT+*U* has found great success due to its computational inexpensiveness.[97]

A computationally more expensive alternative to DFT+*U* are hybrid functionals. They combine a portion of the exact exchange from Hartree−Fock and another part from LDA or GGA. The reasoning behind this is that they strive for an error cancellation of overdelocalized DFT and under-delocalized HF calculations. Unfortunately, this is a computationally very expensive method when used in a plane-wave periodic system (for molecular systems using atomic orbitals, it is more efficient). The accuracy depends on the functional used and the mixing ratio.[105] Nevertheless, hybrid functionals still fail at estimating the band gap for materials with very high and very low values.[106] Hybrid functionals are, strictly speaking, not an ab initio approach because the percentage of HF exchange they use had been chosen arbitrarily (usually by fitting).

Among the most commonly used functionals are B3LYP, PBE0,[107] and HSE, which give fairly good estimations of the band gap, as shown by Marques et al.[106] PBE0 incorporates 25% of the global HF exchange, which is a good compromise for most materials. However, it fails to properly describe very small or very large band gap materials. For small band gap materials, the optimal HF exchange would have to be around

https://dx.doi.org/10.1021/acscatal.0c02557
ACS Catal. 2020, 10, 14984−15007

12% and for large-band gap materials around 70%.[106] HSE06[108] also incorporates 25% of HF mixing (short-range only, not global) and uses an error-function screened Coulomb potential. It splits it in the short-range (SR) and long-range (LR), modestly decreasing the computational time in comparison with other hybrid functionals. The SR form of the functional is evaluated with HF, while the LR is treated with PBE-GGA.[109] Vydrov et al.[110] illustrated that the SR term is responsible for the improved thermochemical results. The Becke-3-Lee-Yang-Par (B3LYP)[87,111] functional is often the most used hybrid functional in molecular calculations, also including 25% global HF exchange. Although it predicts the properties of molecules very well, it fails for periodic systems as demonstrated by Paier et al.[112] This is due to B3LYP failing to describe the transition from localized electrons to delocalized electrons (metals). The error is normally larger than 25%, while for the transition and noble metals it approaches 40%. However, B3LYP can still be applied to nonmetallic systems, whereas it has proven to properly describe some materials with antiferromagnetic insulating ground states (e.g., NiO, MnO, CoO).[113,114] Consequently, HSE06 and PBE0 are the most predominantly used hybrid functionals, as shown in Table 1.

A comprehensive study and comparison of the predictions of DFT+*U* and hybrid functionals, particularly the effect of the Hubbard term on the band gap and reaction barriers, was conducted by Verma et al.[101] The authors concluded that the *U* value has a big impact but is required only for atoms with d (and f) orbitals. Loschen et al.[115] compared the LDA+*U* and GGA+*U* approach on CeO_2 and Ce_2O_3 and further confirmed that the *U* value for cerium is not transferrable between different materials and some materials (Ce_2O_3) are more sensitive to this value than others (CeO_2). Although LDA in general performs much more poorly than GGA, they demonstrated that in some cases LDA+*U* is better due to a fortuitous error cancellation.

It should be noted that DFT describes the ground state. Although it is often used to estimate the band gap and even the potential energy surface of excited species, these values have, strictly speaking, no physical justification. The excited states are more correctly described by the time-dependent DFT (TD-DFT), which can yield information on absorption spectra, as well.

TD-DFT is used to investigate systems in excited states. Upon the absorption of a photon, the system is not in a stationary state. According to Kasha's rule, only the lowest excited state of a given multiplicity are relevant for fluorescence or phosphorescence. Structural (nuclear) relaxation of the excited system to a S_1 minimum is followed by fluorescence back to the ground state S_0 or an intersystem crossing (from singlet to triplet), which exhibits phosphorescent relaxation. TD-DFT is useful to investigate the energetics of the system on the S1 plane, including excited state barriers and conical intersections.

Other methods include GW approximation,[116] which yields good results for bandgaps, and the Bethe-Salpeter (BSE)[117] equation for absorption spectra. These methods are often forgone due to their exceptional computational cost and because they cannot yield thermodynamic properties or structures for they do not give total energies. Thus, most research is predominantly done using DFT.

DFT can be used to study the stability of the surfaces, to predict the adsorption energies of different species on active sites, and to perform a mechanism and kinetic analysis with respective energy barriers. Most authors focus their work on experimental findings, while theoretical investigations usually focus on adsorption, reactions thermodynamics and occasionally the identifications of transition states, band gap and overall band structure, density of states, position of conduction and valence bands, charge transfers, and ionization potentials are the most important. Very rarely are electron excitations and other photoinduced effects rigorously accounted for.

As discussed above, the accuracy of the DFT method, the elusive chemical accuracy, depends hugely on the functional used. While a true chemical accuracy seems out of reach, qualitatively reasonable results and correct trends are not, provided a suitable functional for the problem at hand used. In ab initio studies, the most used GGA functional has been that of Perdew, Burke, and Ernzerhof[118] (PBE) despite all the GGA-related shortcomings.

3.2. Kinetic Modeling. A multiscale model aims to describe the reaction at several (at least two) size- and time-scales. On the electronic scale, quantum approaches (most commonly (TD-)DFT) are used to obtain potential energy surfaces at the ground state S_0 and excited state S_1 (adsorption energies, reaction energies and barriers, tunnelling factors, etc.). Subsequently, first-principles kinetics can be extracted using a variant of the transition state theories, followed by kinetic modeling such as microkinetic modeling or kinetic Monte Carlo (kMC) simulations, which can be used to obtain the kinetics of the system.

In microkinetic modeling, a set of differential equations is solved, describing the catalyst surface, gaseous phases, and, if relevant, liquid phase and interfaces. A set of differential and algebraic molar balance equations is written for every species in the corresponding phase(s) and for the balance of vacant active site(s). Usually, competitive adsorption, desorption, lateral interactions, and surface transformations are included.

For photocatalytic reactions, irradiation must also be modeled. Since 1960, the radiation transport equation (RTE) has been widely used for modeling the light adsorption in photoreactors. Also, the excitation of individual species from S_0 to S_1 and their transformations must be described. Microkinetic modeling is not computationally demanding and allows for a quick sweep over several reaction and reactor parameters. However, it lacks the capabilities to probe the catalyst surface on the atomistic level. As it deals with averages, it cannot include the effects of adsorbate relative positions, such as lateral interactions and cooperative effects.

On the other hand, kinetic Monte Carlo (kMC) can be used to obtain detailed insight into the evolution of the catalyst surface. It is a stochastic numerical method to solve the master equation. It describes a system with a state vector and time. The probability that the system exists in a given state is proportional to its energy in a Boltzmann fashion. This probability is only dependent on the previous state and not on the states leading up to it. Thus, for any given state of the system, a list of permissible reaction steps and their probabilities (proportional to their rates) can be collated. A step is then randomly chosen, and the time is advanced inversely proportionally to the rate of the step. At each step, the exact configuration of the surface is evaluated and the reaction rates accordingly modified as necessary (for instance taking lateral interactions explicitly into account). While kMC is much more computationally demanding than simple microkinetic models, it offers an additional level of insight and is the most commonly used statistical technique for

https://dx.doi.org/10.1021/acscatal.0c02557
ACS Catal. 2020, 10, 14984−15007

treating spatiotemporal events because of the complexity of real systems. When lateral interactions between the adsorbates are strong, microkinetic models may suffer from inaccuracies, whereas a kMC simulation will give correct results,[119] as demonstrated by Andersen et al.[120]

3.3. Macroscale Simulations. On the macroscale, computational fluid dynamics (CFD) is usually employed to study the fluid flow, pressure drop, reactor shape, catalyst loading, and other real-life parameters of the reaction vessel. CFD hinges upon solving the Navier−Stokes equation, which yields the velocity field, which is coupled with the reaction mechanism. Once the velocity field is calculated, other quantities of interest (temperature, pressure) at each point in the mesh are calculated (temperature, pressure, concentrations). Linking CFD with kinetic simulations allows for a recalculation of the reaction parameters for each point in time and space, explicitly taking the reactor type and subsequent heat and mass transfer effects into account.

Reactions can proceed in slurry reactors, fixed bed reactors, or membrane reactors. Such theoretical simulations, although possible and executed on simple thermocatalytic systems, remain to be implemented for photocatalysis. Currently, CFD-only description (no multiscale) has been performed for CO_2 photoreduction. Despite the design of photoreactors being equally important as the quantum description of the reaction and catalyst screening, this area of research has received considerably less attention.[121]

4. CALCULATED ELECTRONIC PROPERTIES

Most theoretical studies investigate electronic properties, while the treatment of reaction mechanisms (vide infra) is much rarer. In this section, we present an overview of the theoretical studies of photoactivation of CO_2 on heterogeneous catalysts.

Ghuman et al.[72] investigated the effects of monodoping and codoping of amorphous TiO_2 on its electronic properties. Through calculating the band gap, total density of states (DOS) and projected density of states (PDOS), the authors concluded that doping in any form reduces the band gap of the material. However, monodoping also resulted in a decrease of photocatalytic activity. PDOS (projected DOS) of N-doped aTiO_2 showed that the p states of N are influencing the energy band structure because of the upshift of the tail of VB maxima, while also being responsible for the intermediate energy band found 0.95 eV below CB. It was found that this midgap state localizes charge carriers and results in the reduction of charge migration, acting as a recombination center.[122] A midgap state is also present in Nb-doped aTiO_2, lying 0.5 eV below CB with a width of 0.3 eV. These midgap states do not improve the photocatalytic activity because the charge localization is larger than in pristine aTiO_2, suggesting that these midgap states act as recombination centers and are reducing the charge carrier mobility. To tackle this problem, the authors codoped their *a*-TiO_2, using both Nb and N, to introduce charge compensation and delocalize photogenerated charge carriers, effectively improving photocatalytic activity. This happens because the charge compensated codoped system shifts the acceptor states toward the VB edge, while the donor states are shifted toward the CB edge.[123]

Liu et al.[124] investigated the local density of states (LDOS) of adsorbed CO_2 on Zn_2GeO_4. The authors first calculated the band structure of pristine Zn_2GeO_4 and then proceeded to incorporate defects into the catalyst studying their effects on the adsorption of CO_2. LDOS revealed a strong bonding between C and the surface O, which is attributed to a significant overlap between the atomic orbitals of C and O. They also observed an interaction between O from CO_2 and Ge, suggesting a strong interaction of CO_2 with Zn_2GeO_4. The strongest adsorption of CO_2 on the pristine (010) surface was −1.04 eV and increased to −1.28 eV on the defective surface (oxygen vacancy), while on the (001) surface introducing an oxygen vacancy increased the interaction from −1.12 to −2.17 eV.

Hahn et al.[125] investigated the adsorption and activation of CO_2 on a CeO_2 surface. They compared the partial density of states (PDOS) of free CO_2 and of linear, monodentate, and bidentate adsorbed geometries of CO_2. The PDOS calculation revealed that in the linear configuration of CO_2, it exhibits the same PDOS as a free CO_2 molecule, meaning that the weak interaction is purely physisorption. The most stable adsorption was in the monodentate configuration with an adsorption energy of −0.31 eV, while the bidentate configuration appears to be closer to linear adsorption with the value of −0.12 eV, suggesting physisorption. These results apply for a 1/9 ML coverage, while at higher coverages, physisorption predominates because of stronger interactions between neighboring molecules. The calculated band gap of CeO_2 (111) was 1.99 eV.

Wang et al.[126] investigated the doping and N vacancies effects on C_3N_4 (not to be confused with g-C_3N_4). They concluded that simultaneous doping with K and B, while also incorporating N vacancies into the material, lowers the band gap of the material. In 5% KBH-C_3N_4, the band gap was lowered to 1.74 eV from 2.74 eV in pristine C_3N_4. TDOS and PDOS were also computed, indicating that there was a midgap state present in the doped C_3N_4 acting as a recombination center. Further analysis revealed that K and B do not significantly contribute to the formation of the midgap state. LUMO and HOMO were also calculated and were found to be mainly constituted by the N 2p and C 2p orbitals, respectively. The Bader analysis concluded that the K and B atoms act as electron donors with Δq values of −1.55 and −2.10, respectively, while the N atoms act as electron acceptors with a Δq value of 1.37.

Chang et al.[127] performed calculations on a theoretically feasible material, which was proposed from first-principles based on the success of g-C_3N_4, namely a new metal-free catalyst B_4C_3. After calculating that the material is experimentally feasible, they performed further electronic calculations to predict its characteristics. The calculated band gap was 2.39 eV. The calculated band diagram and PDOS suggested a spatial separation of the photoinduced electrons and holes, which should inhibit charge recombination.

Tafreshi et al.[45] calculated the band structure and band gap for a hybrid material Ag_3PO_4(111)/g-C_3N_4. The hybrid lowers the band gap of 2.52 eV compared with the pristine Ag_3PO_4 (111) and g-C_3N_4 with a band gap of 2.75 and 3.13 eV, respectively. PDOS and TDOS unveiled that CBM is mostly governed by the g-C_3N_4 atomic orbitals; meanwhile, the VBM is dominated by the atomic orbitals of Ag_3PO_4 (111).

Homlamai et al.[21] investigated the adsorption of CO_2 and the reaction mechanism on several metal (Fe, Ni, Cu, Co) g-C_3N_4, which we discuss in the respective sections. From PDOS, the authors determined that Fe-*g*-C_3N_4 should in theory display the highest adsorption energies since the atomic overlap between the metal d-orbitals and the CO_2 p-orbitals was the highest. The band gap calculations were also

https://dx.doi.org/10.1021/acscatal.0c02557
ACS Catal. 2020, 10, 14984−15007

performed and showed that incorporating metal atoms reduces the band gap significantly. The band gap values for g-C_3N_4, Fe−C_3N_4, Ni−C_3N_4, Co−C_3N_4, and Cu−C_3N_4 were 2.90, 1.31, 0.79, 0.98, and 0.99 eV, respectively.

Li et al.[128] studied a GaP/TiO_2 heterostructure, where an unstable GaP surface is coated with TiO_2. The authors calculated the band gap and DOS. The band gap value was reduced to 1.5 eV (relative to pristine GaP with a band gap of 2.26 eV), which was attributed to the GaP increasing VBM of the heterostructure, shown by DOS. Furthermore, it was found that the heterostructure promotes charge carrier separation because of the electrons having their lowest energy states in TiO_2, while the photoinduced hole remained in GaP.

Wang et al.[31] took a closer look at S-doped g-C_3N_4. They found that PBE-GGA calculations significantly underestimated the band gap. The experimental value was 2.55 eV, while the calculated value was only 1.18 eV (see discussion in the previous subsection). TDOS and PDOS were also calculated, showing that the incorporation of a sulfur atom into the matrix brought an extra electron, consequently introducing spin polarization.

A different study of S doped g-C_3N_4 was performed by Wang et al.,[129] where a hybrid functional (HSE06) was used, which yielded a much better agreement with the experimental value. The calculated band gap was 2.42 eV (experimental: 2.55 eV). In pristine g-C_3N_4, HOMO is mostly localized on N atoms, whereas LUMO comprises mostly C atoms. Upon doping with S, HOMO mostly moves to N atoms, while LUMO is located on S atoms, indicating a better charge separation. The authors also calculated the band edge for both catalysts using the work function. The resulting values for CBM were −1.05 and −1.11 V for g-C_3N_4 and S-doped g-C_3N_4, respectively, which is above the CO_2/CH_3OH potential. The VBM values were calculated to be 1.75 and 1.31 V for g-C_3N_4 and S-doped g-C_3N_4, respectively, which is below the CO_2/CH_3OH potential. This indicates that both are capable of reducing CO_2 to methanol, with the S-doped g-C_3N_4 having a slightly higher (for 0.06 V) located CBM than g-C_3N_4.

As discussed in the previous section and seen here (see also Table 1), hybrid functionals are necessary for a proper electronic structure description. The general trend is that doping reduces the band gap, which is favorable for visible light absorption.[72,126] However, doping might not only decrease the band gap but also introduce a midgap state into the catalyst electronic structure. The reports on its effect vary. While some midgap states might promote photocatalytic activity, it seems that others can act as recombination centers, hindering the activity.[52,53] Doping the catalyst, where codoping offers the best results;[72] deposition of a cocatalyst, which acts as an electron sink and prevents the charge recombination and promotes the charge transfer; or the so-called Z-scheme photocatalysts, where a combination of photocatalysts is used to produce higher energy excited electrons, are the most promising trends. Recently, there have been studies where novel photocatalysts are identified by a purely ab initio approach, solidifying the importance of the theoretical search for new photocatalysts. A prime example of such a photocatalyst has been the discovery of g-C_3N_4, which has been in recent years investigated as a strong competitor to the traditional TiO_2. Other purely theoretical studies have hinted at other novel materials, such as B_4C_3.[127]

5. ADSORPTION

As succinctly described by Sabatier, the interaction between the catalyst and the substrate must not be too strong nor too weak for optimal catalysis. Thus, we first turn our attention to the adsorption of CO_2 on catalytic surfaces, which is, for obvious reasons, theoretically the most thoroughly studied part of the reaction cascade.

CO_2 is an inert and very stable compound with a formation energy of −393.5 kJ mol^{-1}. Because of its geometry (O═C═O angle is 180°, C═O bond length is 1.16 Å), the molecule is not polar. While the reduction potential of CO_2/CO_2^- vs NHE is −2.22 V, it can be changed by adsorption (−1.98 V on anatase TiO_2(101)).[130] In this section, we review the calculated adsorption values of CO_2 on different photoactive substrates.

Ye et al.[131] studied its adsorption on In_2O_3. Three stable adsorption configurations were tested, the most stable one having an adsorption energy of −1.25 eV. The bond angle in CO_2 was reduced to 126°, and the bonds were elongated to 1.29 and 1.28 Å. The Bader charge analysis showed that the electron density moved from In_2O_3 to CO_2.

Hahn et al.[125] investigated the CeO_2 (111) surface at different coverages and configurations. The monodentate, bidentate, and linear CO_2 adsorption modes were investigated at coverages 1/9 ML, 1/2 ML, and 2/3 ML. At a 1/9 ML coverage, the monodentate configuration had the strongest interaction, followed by the bidentate and linear, with values of −0.31, −0.12, and 0.02 eV, respectively. In the monodentate configuration, the C═O bond length is elongated to 1.27 Å, and the bond angle is 129.7°. However, in the bidentate configuration, the bond lengths are 1.22 and 1.30 Å, and the bond angle is 129.2°. In the linear configuration, no significant bond elongation or bending (O═C═O: 177.6°) is found because of weak interaction with the surface. At higher coverages (1/2 ML and 2/3 ML), the interaction of CO_2 is decreased because of the repulsion between the CO_2 molecules.

He et al.[130] conducted a theoretical study of CO_2 adsorption on a pristine and oxygen-vacant anatase (101) surface. On the pristine anatase surface, they identified four possible configurations of adsorbed CO_2 with two of them being favorable: a linear configuration and a bidentate one. In the linear configuration, the bonding strength was −0.20 eV, and in the bidentate configuration, it was −0.14 eV. Such low values, which are characteristic of physisorption, were attributed to the use of a vanilla PBE functional by the authors. The oxygen-deficient (reduced) anatase (101) surface proved to be a better alternative for photocatalysis with a more favorable interaction of CO_2 in the linear configuration (−1.09 eV) than in the bidentate configuration. In both cases, the molecule is bent as the oxygen from CO_2 is pushed toward the oxygen vacancy, decreasing the angle to 128.7° and elongating the bonds to 1.20 and 1.34 Å, respectively. The authors emphasize that the binding energies of O_2 and H_2O are even more favorable, meaning these species might compete for the oxygen vacancy sites, effectively poisoning the catalyst.

Liu et al.[132] also investigated the adsorption of CO_2 on the oxygen-vacant anatase (101) surface. However, their calculations were done using the DFT+*U* approach. The strongest binding was found for the linear configuration (−0.89 eV), while in the vertical configuration CO_2 binds somewhat less strongly (−0.65 eV). On the stable pristine TiO_2 (101)

https://dx.doi.org/10.1021/acscatal.0c02557
ACS Catal. 2020, 10, 14984−15007

surface, the binding interaction is −0.45 eV. Qualitatively, the results match those of He et al.[130]

Hammami et al.[133] conducted an extensive study on the (001) surfaces of different metal oxides (Ca, Sc, Ti, V, Cr, Mn, Fe, Co, Ni), systematically testing different adsorption modes: vertical, flat (the oxygen atoms above two metal cations, the carbon in the gap between the surface oxygen atoms), BA1 (C atop of the surface oxygen and the CO_2 oxygen atoms between two metal ions), and BA2 (C atop of the surface oxygen and the CO_2 oxygen atoms atop of the metal atom). In most cases, the flat configurations proved to be the most favorable for adsorption. However, there were some exceptions, such as FeO, which favored BA2, or CaO with BA1. The strength of the adsorption spanned from 2.09 to 0.10 eV, as follows: Sc > V > Ti > Ca ≫ Cr > Fe > Co > Mn.

Jensen et al.[134] studied various MgO and CaO sites. The most favorable adsorption sites on MgO proved to be the step and corner (tridentate) with adsorption energies of −1.60 and −1.58 eV, respectively, followed by the corner bidentate configuration with an adsorption energy of −1.19 eV. The corner (monodentate) and step sites were also the most favorable on CaO with adsorption energies of −2.30 and −2.27 eV, respectively, followed by the corner (bidentate), corner (tridentate), and terrace site with values of −1.89, −1.70, and −1.00 eV respectively. As previously reported, the bonds in CO_2 were also elongated and the angle decreased.

Saputro et al.[135] reported the adsorption modes of CO_2 on Pd_6M clusters doped by transition metals (M = Ni, Cu, Pt, Rh, and Pd). It was determined that CO_2 binds in the bidentate configuration in all instances. The charge transfer analysis between the cluster and CO_2 showed a positive correlation between the amount of the charge transfer and the adsorption strength. In the cases of Ni and Cu, the adsorption is stronger (−0.43 eV, −0.47 eV, respectively) as the d-orbitals of the cluster interact with the LUMO orbital of CO_2. Consequently, the C═O bonds elongate, and the molecule bends.

Cao et al.[34] investigated the adsorption on g-C_3N_4 supported Pd (100) and Pd (111). The investigation revealed that the Pd (111) surface binds CO_2 stronger than Pd (100). They also showed that the desorption of products plays a role in selectivity. Methanol has a lower adsorption energy on Pd (111) than on Pd (100), which could promote its production. Zhu et al., however,[136] thoroughly looked into the adsorption solely on g-C_3N_4, considering all possible sites and taking into account all possible orientations. They showed that the horizontal adsorption is preferred, although by a small margin (0.04 eV between the most stable vertical and horizontal adsorption). The adsorption interactions are −0.42 eV or less.

The adsorption energies of CO_2 on pristine and defective Zn_2GeO_4 were studied by Liu et al.[124] using the PW91 GGA approach. For the pristine surface, the (010) and (001) planes were studied because they are the most common and active. Five different CO_2 configurations were chosen and studied: vertical, horizontal (monodentate), bidentate, and two bridge configurations (the carbon atom bent toward the surface or outward). On the (010) plane, the most stable was the bridge configuration (inward) with an adsorption energy of −1.04 eV, followed by the bidentate configuration (−0.91 eV). For the (001) plane, the bridge (inward) configuration was the most stable with an adsorption energy of −1.12 eV. In all cases, the bonds were elongated and the molecule was bent as the electron density flowed from Zn_2GeO_4 toward CO_2. Introducing an oxygen vacancy slightly increases the adsorption interaction by 0.14 and 0.24 eV for the (010) and (001) surfaces, respectively. It is possible to heal the oxygen vacancy by the dissociative adsorption of CO_2.

An interesting material is boron in the B_{80} fullerene structure, which has a great potential for metal-free photocatalysis. Qu et al. studied the adsorption of CO_2 on B_{80}[137] and compared three possible adsorption modes. In all instances, one oxygen was bound in the bidentate configuration. As B_{80} consists of both acidic and basic sites,[138] CO_2, being a Lewis acid, can interact strongly with the basic sites of B_{80}. This is confirmed by the strong adsorption energies in all three configurations (−0.64, −0.64, and −0.62 eV). As discussed later on, the authors also showed that B_{80} can function as an efficient catalyst for the production of HCOOH.

As shown, adsorption depends on several parameters, namely, the catalyst structure, doping or presence of a cocatalyst, the surface facet, and defects (e.g., oxygen vacancies). The general trends demonstrate that horizontal adsorption is favored over vertical,[132] whereas oxygen vacancies, depositions of cocatalysts, and doping increase the adsorption strength relative to pristine surfaces.[130] Lower surface coverages result in increased interactions because of a weaker repulsion between neighboring CO_2 molecules.[125] When CO_2 is activated upon adsorption (Figure 3), which is

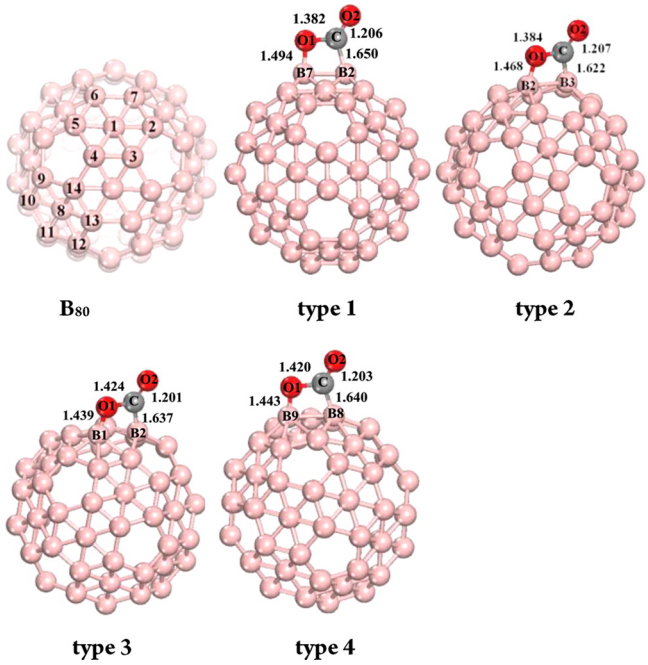

Figure 3. Visual representation of the B_{80} cluster and different types of CO_2 adsorption on its surface. Color code: pink − B, gray − C, red − O. Reprinted with permission from ref 138. Copyright 2014 American Chemical Society.

evidenced by the elongation of the bond (decrease of the bond order) and the electron transfer from the catalyst to the LUMO of CO_2 (Figure 4),[139,140] it bends the molecule by the excess electron density.

Adsorption and a consequent activation of the CO_2 molecule is an important first step in the reaction. The interaction of other species with the catalyst (i.e., adsorption/desorption) also plays a significant role in determining the selectivity and should not go unmentioned. If intermediates bind to weakly they can desorb before being converted to the

https://dx.doi.org/10.1021/acscatal.0c02557
ACS Catal. 2020, 10, 14984−15007

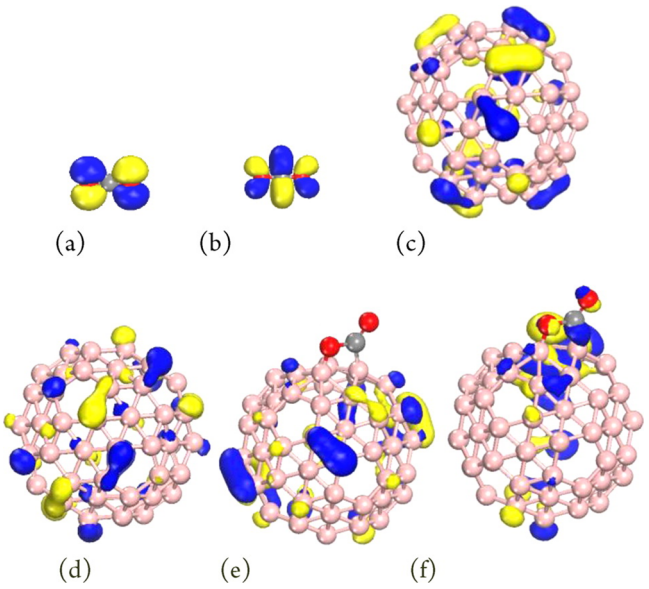

Figure 4. (a) HOMO and (b) LUMO of gaseous CO_2; (c) HOMO and (d) LUMO of B_{80}; (e) HOMO and (f) LUMO of chemisorbed CO_2 on B_{80} in the most stable configuration. Color code: pink − B, gray − C, red − O. Reprinted with permission from 138. Copyright 2014 American Chemical Society.

final products. Conversely, the final products should not bind strongly to avoid further conversion or reverse reactions. This was demonstrated by Cao et al.[34] who studied the photoreduction of CO_2 on Pd(100) and Pd(111) on g-C_3N_4. They found that the adsorption interaction of methanol on Pd(100) is 10-times stronger than on the Pd(111) surface, making desorption from Pd(111) much faster. Since the methane desorption energies are comparable on both surfaces, they concluded that Pd(111) is most likely more selective toward methanol. Similarly, Qu et al.[137] demonstrated the importance of the adsorption interaction of products on B_{80} fullerene. Their results indicated that CO binds very strongly and is highly unlikely to be a major product, while CH_4, CH_3OH, and HCOOH display a weaker adsorption. Combining that with the limiting potentials, they concluded that HCOOH is favored. The product distribution is highly dependent on the desorption rates of intermediates and products. Weaker adsorption of important intermediates, such as CO and HCOOH, might prevent the formation of hydrocarbons because of their tendency of desorption from the surface, whereas stronger adsorption may imply that no CO and HCOOH is produced. Adsorption is an important step, which is dependent not only on the catalyst and its modifications but also on the exposed surface.

6. REACTION MECHANISMS

CO_2 can be reduced to several carbon-containing species, such as CO, HCOOH, CH_3OH or CH_4. From the thermodynamic point of view, the formation of multielectron reduced species is easier than the formation of CO_2^-, which is exploited in electrocatalysis. However, kinetics also plays an important role in the product distribution. The reduction potentials (vs SHE at pH = 7 and 25 °C) are, as follows:

$$CO_{2(g)} + e^- \Leftrightarrow CO_{2^-(aq)} \quad -1.99V$$

$$CO_{2(aq)} + e^- \Leftrightarrow CO_{2^-(aq)} \quad -1.90V$$

$$CO_{2(g)} + 2H^+_{(aq)} + 2e^- \Leftrightarrow HCO_2H_{(aq)} \quad -0.61V$$

$$CO_{2(g)} + 2H^+_{(aq)} + 2e^- \Leftrightarrow CO_{(g)} + H_2O_{(l)} \quad -0.52V$$

$$CO_{2(g)} + 4H^+_{(aq)} + 4e^- \Leftrightarrow H_2C(OH)_{2(aq)} + H_2O_{(l)} \quad -0.49V$$

$$CO_{2(g)} + 6H^+_{(aq)} + 6e^- \Leftrightarrow CH_3OH_{(aq)} + H_2O_{(l)} \quad -0.38V$$

$$CO_{2(g)} + 8H^+_{(aq)} + 8e^- \Leftrightarrow CH_{4(g)} + 2H_2O_{(l)} \quad -0.24V$$

The reduction potential at the catalyst must be lower than the desired product for the reaction to proceed as depicted in Figure 5. As seen in the above overall net reactions, different species require a different amount of electrons to be formed.

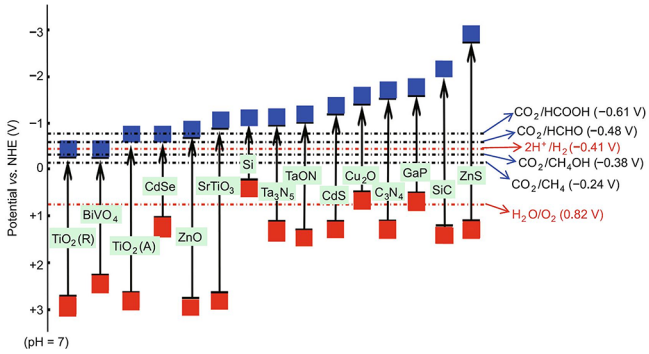

Figure 5. Reduction potentials for different products and corresponding reduction/oxidation potentials from several photocatalysts. Reprinted with permission from ref 155. Copyright 2014 Springer.

The process consists of several elementary steps and is rather complex (vide infra). Another important aspect of the reaction mechanism is the choice of the reducing agent. The most commonly used ones are H_2O and H_2; however, sometimes CH_4 and CH_3OH are also used.[14,156,157] H_2O has the obvious advantage of high abundance and low price and is therefore widely used. However, it has a few disadvantages, such as competitive reactions (water splitting)[158] due to its high adsorption affinity, covering many active sites, and hindering the reduction of CO_2.[159] The oxygen released from the oxidation of water can also retard its photocatalytic ability and even help form CO_2.[160]

A possible solution might be to use H_2, which yields similar products through a different mechanism depending on the reaction system. Because no oxygen is produced, the H_2 pathway also enables higher yields.[161] The reaction mechanism, pathway, kinetics, and products are of course specific to each studied system.

In Table 2, we list the most commonly used photocatalysts for the reduction of CO_2 with H_2 or H_2O and the obtained products. However, the challenge remains to postulate a single reaction mechanism to describe the photocatalytic reduction of CO_2. Most research is focused primarily on the experimental determination of catalyst properties and yields.

Cao et al.[34] investigated the photocatalytic reduction of CO_2 on Pd/g-C_3N_4 and calculated the adsorption energies. By means of FTIR, they proposed a simple reaction mechanism, which suggested that electrons accumulate on the Pd particles. They react with the adsorbed CO_2 molecule to form HCOOH,

https://dx.doi.org/10.1021/acscatal.0c02557
ACS Catal. 2020, 10, 14984−15007

Table 2. Most Common Catalyst/Reactant Combinations for Photocatalytic CO_2 Reduction and Corresponding Products

reactant	catalyst	products	production [μmol $g^{-1}h^{-1}$]	selectivity	reference
H_2	10 wt %MMT/TiO_2	CO	25.95	98% CO	162
		CH_4			
		C_2H_6			
H_2, heat (190 °C)	$In_2O_{3-x}(OH)_y$	CO	153		18
H_2, heat (170 °C)	ncSI:H	CO	17		163
H_2	0.1 wt %Pd/Nb_2O_5	CO	1880	99.5% CO	23
	10 wt %Pd/Nb_2O_5	CO	750		
		CH_4	110		
H_2, heat (150 °C)	0.03%Bi/$In_2O_{3-x}(OH)_y$	CO	1.32		164
H_2O(g)	S-doped g-C_3N_4	CH_3OH	1.12		31
	undoped g-C_3N_4	CH_3OH	0.81		
H_2O(g)	Pd(100) g- C_3N_4	CH_4	0.29		34
		CH_3OH	2.23		
	Pd(111) g-C_3N_4	CH_4	0.4		
		CH_3OH	3.17		
H_2O(g)	2.5%$CuInS_2$/TiO_2	CH_4	2.5		165
		CH_3OH	0.86		
H_2O	C/Pt/In_2O_3	CO	126.6		79
		CH_4	27.9		
H_2O	0.5%GDY/TiO_2	CO	50.53		166
		CH_4	30.92		
H_2O	1% Pt/TiO_2	CH_4	4.6		167
H_2O(g)	1.5%Ag/TiO_2	CH_4	1.5		24
H_2O	1.5%Ag/TiO_2	CH_3OH	4.5		
H_2O(g)	Au/TiO_2	CH_4	2.52		168
		C_2H_6	1.67		
H_2O(g)	5%Pg-C_3N_4/Sn_2S_3-DETA	CH_4	4.93		169
		CH_3OH	1.35		
H_2O	Bi_2MoO_6 NS	CO	3.62		17
H_2O	$Bi_{24}O_{31}Cl_{10}$	CO	0.9		55
H_2O	3%KBH-C_3N_4	CO	1.19		126
		CH_4	0.63		
H_2O	CeO_x-S/$ZnIn_2S_4$	CO	180		28
H_2O	4.6%Au/ZnO	CH_4	21		170
		C_2H_6	27		
	1.7%Ag/ZnO	CH_4	25		
	1.9%Pd/ZnO	CH_4	18		

HCHO, CH_3OH, and CH_4 in this order. The final product can be very dependent on the exposed surface of the Pd nanoparticles. As methanol appears to have a lower adsorption energy on the Pd (111) plane than on Pd (100), it can desorb more easily before it can react further to CH_4, increasing the selectivity toward CH_3OH. However, the kinetics was determined purely experimentally and no attempt at identifying any transition states was made.

Gao et al.[38] researched Pd/g-C_3N_4 and Pt/g-C_3N_4 solely from the theoretical perspective, treating Pd and Pt as single atoms, which significantly reduces the band gap (from 2.98 to 0.64 and 0.72 eV, respectively) and depresses the conduction-band minimum to −0.9 eV, which is more negative than of CO_2/HCOOH, CO_2/CH_3OH, and CO_2/CH_4. They used the PBE functional with Grimme's empirical corrections (HSE06 was used for the band structures and optical absorption spectra). They calculated the complete potential energy surface along with all transition states for the hydrogenation of CO_2. In this study, the metal atoms function as the active sites, while g-C_3N_4 serves as the source of hydrogen. On Pd/g-C_3N_4, HCOOH and some CH_3OH are predominantly formed, while on Pt/g-C_3N_4 methane forms. In both cases, the proposed reaction pathway follows the following intermediates CO_2 → HCOO → HCOOH → HCO → CH_2O → CH_2OH. It can then dissociate to CH_2 and through CH_3 yield CH_4 or hydrogenate to CH_3OH. On Pd/g-C_3N_4, the first rate-determining step is the formation of HCOOH (0.46 eV), which then desorbs. For the production of CH_3OH, the calculated reaction barrier is 1.43 eV for the formation of HCO from HCOOH and 1.46 eV for the formation of CH_3OH from CH_2OH. Thus, HCOOH is predicted to be the main product. On Pt/g-C_3N_4, the barriers are lower than any desorption energy and CH_2OH forms, which then follows the route CH_2 → CH_3 → CH_4. The hydrogenation of HCOO into HCOOH is the rate-limiting step in this pathway with a value of 1.01 eV.

Wang et al.[126] proposed a mechanism for the photoreduction of CO_2 on 3% KBH-C_3N_4 based on their experimental work (DRIFT, FTIR, UV−vis). They determined CO_2^-, HCO_3^-, CO_3^{2-}, and HCOO as the intermediates on both pristine C_3N_4 and 3% KBH-C_3N_4 and postulated the following mechanism: CO_2 is reduced to CO_2^-, which can react into HCO_3^- (with OH), CO and CO_3^{2-} (with CO_2^-), CO and OH^- or HCOOH. HCOOH can be further dehydrogenated into HCOO, which can dissociate into CO

https://dx.doi.org/10.1021/acscatal.0c02557
ACS Catal. 2020, 10, 14984−15007

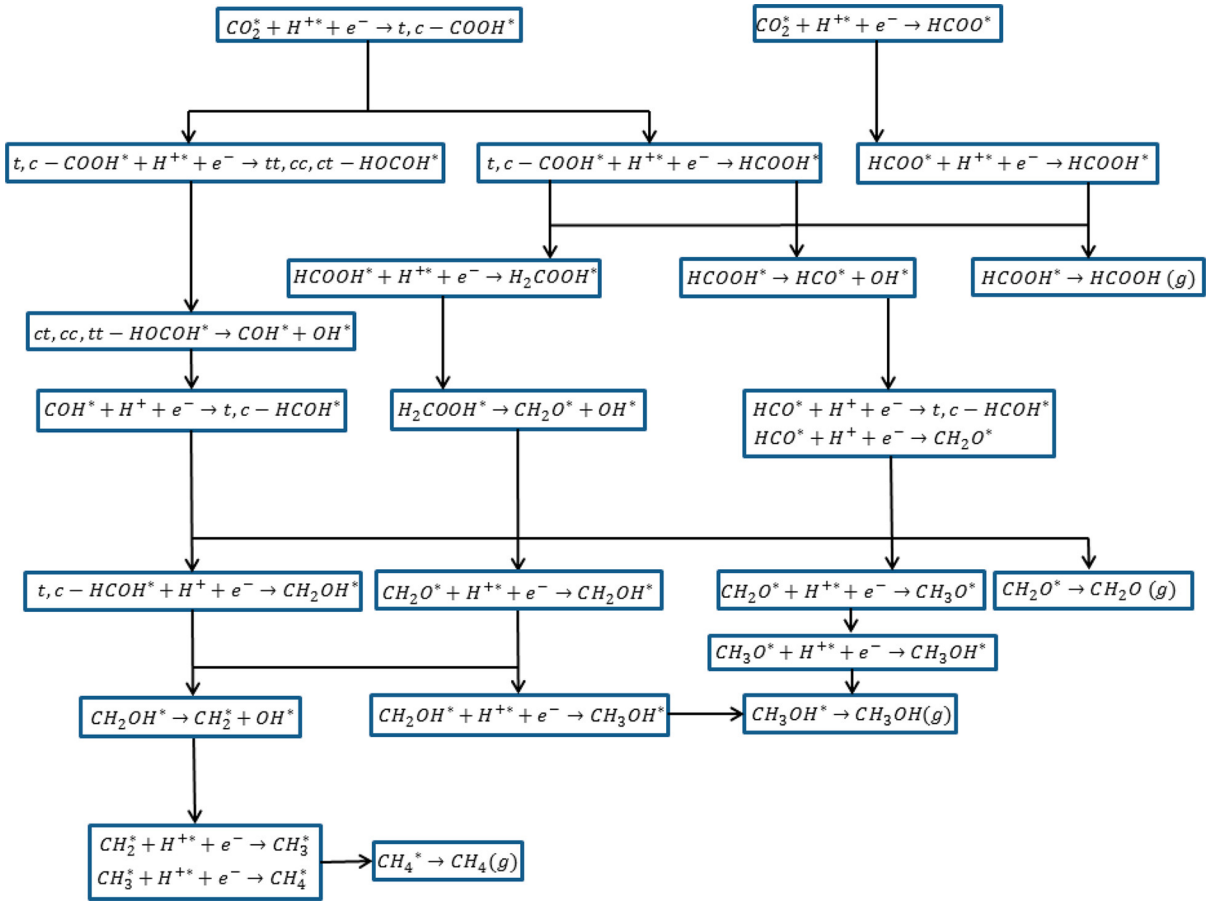

Figure 6. Proposed reaction mechanism with several possible pathways for photocatalytic CO_2 reduction, reprinted with permission from reference 45. Copyright 2019 American Chemical Society.

(and OH). CO can desorb or react further. The C═O bond can be broken (the carbene pathway[171]), producing C and OH in the presence of H^+ and e^-. C is then sequentially hydrogenated CH → CH_2 → CH_3 → CH_4. The major products of the reaction are thus CO and CH_4. The mechanism, however, was not supported theoretically.

Using PBE-GGA based DFT with Grimme's correction (D2), Wang et al.[129] theoretically studied sulfur-doped g-C_3N_4 nanosheets because sulfur enhances their catalytic performance based on electronic and optical properties calculations. For the band gap, PDOS, and absorption spectra calculations, the HSE06 hybrid functional was used. The sulfur doping was found to decrease the band gap from 2.80 to 2.42 eV. While in g- C_3N_4 the Fermi level adjoins the VB, in the doped catalyst the Fermi level moves to the bottom of CB, as in an *n*-type doping system. While investigating the reaction pathway, the authors calculated the Gibbs free energies of the species involved in the reaction. They postulated three reaction pathways, the most probable being: CO_2, COOH, CO, HCO, HCHO, CH_3OH. The rate-determining step was CO_2 → COOH with ΔG = 1.15 eV.

Another study on g-C_3N_4 was done by Azofra et al.,[172] where they studied the reaction mechanism of the CO_2 reduction using PBE-GGA with Grimme's correction (D3). They first examined the stability of planar versus corrugated g-C_3N_4 and showed that the latter was thermodynamically more stable by 2.91 eV. The investigation of the reaction mechanism on the planar and corrugated surfaces yielded the following reaction mechanism: CO_2 → HOCO → CO → HCO → H_2CO → CH_3O → CH_3OH. The rate limiting step in the planar configuration was found to be the first hydrogenation of CO_2 to HOCO with $\Delta G^{298\ K}$ = 1.64 eV, while on the corrugated surface it was significantly lower at $\Delta G^{298\ K}$ = 1.15 eV. The rate-limiting step on the corrugated surface was H_2CO → CH_3O with $\Delta G^{298\ K}$ = 1.21 eV. Planar g-C_3N_4 therefore requires higher overpotentials to initiate the reaction but then quickly reacts toward methanol, while on the corrugated surface it is more likely to see earlier products such as CO (at lower overpotentials). The authors also investigated how the solvent, namely water, affects the reaction mechanism on the corrugated surface. In an aqueous medium, the barrier for the first hydrogenation step is reduced from 1.15 to 0.99 eV, while for the step H_2CO → CH_3O it increases from 1.21 to 1.59 eV.

The reduction of CO_2 on the B_4C_3 monolayer supported on Si was theoretically studied by Chang et al. using the GGA-PBE approach (or HSE06 for band gap calculations).[127] The authors first checked that the monolayer is thermodynamically and kinetically stable, calculating the phonon dispersion and cohesive energy, and performing ab initio molecular dynamics. As the B_4C_3 monolayer can be viewed as an infinite lattice of the $B_4C_3H_6$ molecules (with a tetracoordinated carbon atom in the middle), the electronic structure of the molecule was analyzed. The calculations of the band structure, the projected density of states, dielectric constants, optical absorption, carrier mobilities, and band edge alignments showed that B_4C_3 is a promising material for photocatalysis. The authors calculated

https://dx.doi.org/10.1021/acscatal.0c02557
ACS Catal. 2020, 10, 14984−15007

that the one-electron reduction of CO_2 (to yield CO_2^-) occurs at −1.90 V. However, the proton-coupled conversion of CO_2 requires much more modest potentials: −0.61 V to yield HCOOH and −0.52 V to yield CO (and H_2O). The mechanistic evaluation revealed that CO_2 first hydrogenates to HCOO, then to HCOOH, HCO, CHOH, CH_2OH, CH_2, CH_3, and ultimately CH_4. The rate-limiting step of the reaction is the dehydroxylation of HCOOH to HCO, with a barrier of G = 0.63 eV at 25 °C and 1 atm.

The reaction mechanism of the reduction of CO_2 over $Ag_3PO_4(111)$/g-C_3N_4 was theoretically studied by Tafreshi et al.[45] using the GGA-PBE approach with Grimme's correction (D3). For the electronic properties, hybrid PBE0 and HSE0 were used. They showed that CO_2 is stepwise reduced and can yield HCOOH, CH_2O, CH_4, or CH_3OH. The authors focused on reaction energies (and not barriers) and investigated the complete reaction pathway with all possible intermediates. For the production of methanol, the following mechanism was proposed: CO_2 → HCOO → *t*-COOH → *c*-COOH → HCOOH → HCO → *t*-HCOH → *c*-HCOH → CH_2O → CH_2OH → CH_3O → CH_3OH. The methane pathway branches off at CH_2OH → CH_2 → CH_3 → CH_4. The authors also considered a different mechanism proceeding through HOCOH, which is thermodynamically less favorable. Based on the thermodynamics of the end products, the authors propose that CH_4 is more likely to form than CH_3OH. They also proposed a general reaction pathway for the CO_2 reduction as depicted in Figure 6.

In their B_{80} fullerene study, Qu et al.[137] also proposed a tentative mechanism for the reduction of CO_2, which yields HCOOH, HCHO, or CH_4. As CO_2 can bind to the fullerene in three configurations, they constructed three potential energy surfaces. In all instances, HCOOH was the predominant product with a limiting potential of −0.18 V. Based on thermodynamic considerations (no transition states or kinetics were calculated), CO_2 is reduced to HCOOH via the O═CH−O* intermediate. The formation of more reduced products was deemed less likely.

The reduction of CO_2 was also theoretically studied by Homlamai et al.[21] who studied non-noble metal single-atom catalysts (Fe, Co, Ni) on g-C_3N_4 using the GGA-PBE approach with Grimme's correction (D3). They proposed the following mechanism CO_2 → HCOO → HCOOH and included the transition states in their study. For the first step (yielding formate), the barriers for the reaction were 0.22, 0.60, 1.13, and 0.70 eV on Fe-*g*-C_3N_4, Co-*g*-C_3N_4, Ni-*g*-C_3N_4, Cu-*g*-C_3N_4, respectively. In the second hydrogenation step to form formic acid (HCOOH), the barriers were 0.58, 0.72, 0.34, and 0.02 eV, respectively. Thus, the rate-determining step was the second step for Fe-gC_3N_4 and Co-gC_3N_4 and the first step for Ni-gC_3N_4 and Cu-gC_3N_4. The authors conclude that the activity follows the order: Fe-*g*-C_3N_4 > Co-*g*-C_3N_4 > Cu-*g*-C_3N_4 > Ni-*g*-C_3N_4.

Zhao et al.[170] investigated the reaction mechanism for the CO_2 conversion over noble metals (Au, Ag, Pd) on 3D porous ZnO nanosheets. The authors performed experimental testing and theoretical calculations using the GGA-PBE approach with Grimme's correction (D2). Four reaction mechanisms involving a stepwise hydrogenation of CO_2 were studied: (*i*) CO_2 → HCOO* → H_2COO* → H_2COOH* → H_2CO* → H_3COH* → H_3C* → CH_4, (*ii*) CO_2 →→ H_2COOH* → H_3COOH* → H_3CO* → H_3COH* → H_4COH* → CH_4, (*iii*) CO_2 →→ H_3COOH* → H_3CO* → H_3COH* → H_3C* → CH_4, (*iv*) CO_2 →→ H_2COOH* → H_2CO* → H_3COH* → H_4COH* → CH_4. Additionally, two cross-hydrogenation processes on O and C atoms were also studied: (*v*) CO_2 → COOH* → CO → HCO* → H_2CO* → H_3CO* → H_3COH* → H_4COH* → CH_4 and (*vi*) CO_2 →→ H_3COH* → H_3C* → CH_4. The authors focused on the energetics of the stable intermediates only and did not study the barriers. On bare ZnO nanosheets, the pathway (*iii*) is the most favorable. However, once loaded with metals, the reaction pathway (*v*) also becomes most achievable. This explains why CO and CH_4 concomitantly form. The dehydroxylation of COOH* and H_2COOH* is the rate-determining step, which determines which pathway is predominantly followed. The selectivity can be tuned by balancing between the thermodynamically and kinetically controlled products. On the Pd catalyst, the difference in endothermicity of the dehydroxylations of H_2COOH* and COOH* is the greatest, explaining the high selectivity to CH_4 of Pd-supported catalysts. On the silver catalyst, the formation of CO is preferred. On Au/ZnO, C_2H_6 also forms experimentally but was not theoretically modeled. This reaction is possible by a further conversion CH_4 into C_2H_6 by a dehydrogenative coupling mechanism.[36]

Li et al. investigated the photoreduction of CO_2 on thin TiO_2-coated GaP, which solves the problem of poor stability of pure GaP.[128] With the modified phenomenological theory of Martensitic crystallography and a stochastic surface walking global search, the structure of the interface was resolved on the atomic level as consisting of the (001)TiO_2//(100)GaP, (101)TiO_2//(110)GaP, and (112)TiO_2//(100)GaP junctions with negligible interface strain. The authors showed that the electrons from GaP readily tunnel through a sufficiently thin TiO_2 level, which is responsible for the decrease of the CO_2 reduction barrier from 1.02 eV. While the authors focused mostly on the interface structure and its electronic properties, they also briefly deal with the reaction mechanism. They purport the following mechanism: CO_2 → HCOOH → H_2CO → CH_3OH with the corresponding activation barriers 1.84, 1.82, and 1.24 eV, respectively, when one does not account for quantum tunnelling. When accounted for, the barriers are lowered to more feasible 0.82, 0.80, and 0.28 eV, respectively.

Defective (oxygen vacancy) or pristine TiO_2 surfaces and the reaction mechanisms thereon were theoretically studied by Ji et al.[173] To correctly describe the photogenerated holes and trapped electrons, a combined GGA+*U*/HSE approach was used. The geometries were optimized on the GGA+*U* PBE level and then single point HSE calculations were performed. The authors proposed two tentative mechanisms: fast hydrogenation (CO_2 → CO → CH_2O → CH_3OH → CH_3 → CH_4) and fast deoxygenation (CO_2 → CO → C → CH_2 → CH_3 → CH_4/CH_3OH). The oxygen vacancy was found to be more active than the Ti atoms for the reaction at hand. Based on the calculated transition state barriers, the authors argue that the fast-deoxygenation pathway is unlikely (the key intermediate C* will not form). Instead, a combined mechanism stemming from the fast-dehydrogenation is proposed: CO_2 → CO → HCO → H_2CO → CH_3OH → CH_3 → CH_4/CH_3OH. The rate-determining steps are the reduction of H_2CO to CH_3O (1.26 eV) and the CO_2 dissociation to CO (1.04 or 0.73 eV, depending on the orientation). Because of their strong interaction with the surface, H_2CO and HCOOH are not liberated but react further.

https://dx.doi.org/10.1021/acscatal.0c02557
ACS Catal. 2020, 10, 14984−15007

The reaction mechanisms were studied on a pristine anatase TiO_2 (101) surface by Ji et al.[174] using PBE+U for geometry optimizations and performing single-point HSE calculations for energetics. The authors propose two possible reaction mechanisms (*i*) $CO_2 \rightarrow HCOOH \rightarrow H_2CO \rightarrow CH_3OH \rightarrow CH_4$ and (*ii*) $CO_2 \rightarrow CO \rightarrow H_2CO \rightarrow CH_3OH \rightarrow CH_4$. In (*i*), the rate-limiting step is the photoreduction of $HCOOH \rightarrow H_2CO$ with a barrier of 1.81 eV, while in (*ii*), the rate-limiting step is the dissociation $CO_2 \rightarrow CO$ with a barrier of 1.41 eV. Experimental results show that both routes are active. The oxygen vacancies seem to shift the reaction mechanism from the first pathway, which is typical of the pristine surface, to the second pathway. The authors thus propose a combined reaction mechanism (*iii*) $CO_2 \rightarrow CO \rightarrow H_2CO \rightarrow CH_3 \rightarrow CH_3OH/CH_4$.

Liu et al.[132] also studied the on an oxygen-vacant anatase TiO_2 (101) surface using the DFT+U approach with the PBE functional and the Thatchenko-Scheffler dispersion correction. They showed that after adsorbing on the vacancy site, the CO_2 molecule dissociates to CO and O, filling the oxygen vacancy. The ensuing CO can only bind to another oxygen vacancy and not to the pristine surface. Interestingly, CO_2 can bind in two configurations (vertical and horizontal), of which the horizontal one is more favorable (adsorption energies of −0.89 and −0.63 eV, respectively). However, the barrier for the formation of CO from the horizontal configuration of adsorbed CO_2 is 0.74 eV, but only 0.15 eV from the vertical initial configuration. CO is preferentially bound as a monodentate species, which then proceeds through the $HCO \rightarrow CHOH \rightarrow CH_2OH \rightarrow CH_3OH \rightarrow CH_3O \rightarrow CH_4$. CO can also bind as a bidentate species, which is reduced as $HCO \rightarrow CH_2O \rightarrow CH_3O \rightarrow CH_4$. The formation of methanol is not expected as its desorption energy is 1.66 eV, while the corresponding reaction barrier for the formation of CH_3 intermediate is only 0.18 eV. The authors also considered the C pathway: $CO \rightarrow HCO \rightarrow CHOH \rightarrow CH \rightarrow CH_2 \rightarrow CH_3 \rightarrow CH_4$, where the rate-determining step (CHOH → CH) has a barrier of 1.96 eV.

As described in this section, authors focus on the elementary reactions relevant for their setup and consequently no single study deals with the all-encompassing mechanism of the photoreduction of CO_2. The mechanism also depends on the reactant used and differs between H_2, H_2O, CH_4, or CH_3OH, which can all be used as reductants. Karamian and Sharifnia[175] proposed a general mechanism of photocatalytic reduction of CO_2, which describes the generation of the oxidizing species (holes, hydroxyl radicals, superoxide, and singlet oxygen), the oxidation of the reducing species (usually aliphatics) and the reduction of CO_2 by different reductants. The choice of the reductant also influences the product ratio considerably, which the authors describe in their general mechanism. While the first product in all cases is CO, possible subsequent products include methane and higher hydrocarbons, methanol, ethanol, formic acid, acetic acid, and acetone.[175] In Figures 6 and 7, the theoretical mechanism is depicted. The products obtained in a particular setup depend on the catalyst used (material, thickness, surface treatment, facets, defects), the conditions and the reactants.

Three main reaction mechanisms are proposed. If CO_2 undergoes dissociative adsorption, the ensuing CO is hydrogenated via the fast hydrogenation route through CH_2O to CH_3OH or CH_4. This mechanism is feasible when oxygen vacancies are present on the surface, such as in the O-lean

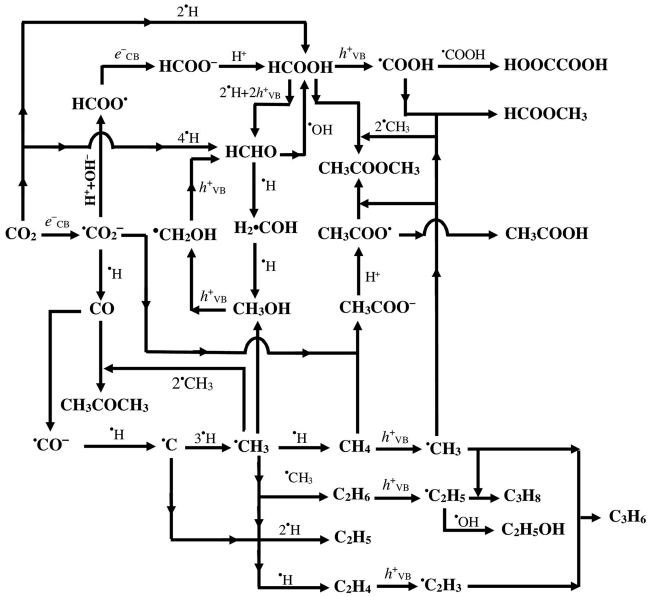

Figure 7. Photocatalytic reaction mechanism of CO_2 reduction in a mixture of reductants, with several possible pathways. Reprinted with permission from ref 175. Copyright 2016 Elsevier.

TiO_2. Most photocatalysts, however, hydrogenate CO_2 to either HCOO (the formate route) or COOH. The former mechanism is generally favored on catalysts with metals (Pt/g-C_3N_4), while the latter occurs more rarely on some less noble metals or nonmetal catalysts. Nevertheless, both mechanisms *can* play a non-negligible part during photocatalysis and should be considered. The summary on the investigation methodologies on several catalysts, and the results are gathered in Table 3.

7. KINETIC MODELING AND MACROSCALE SIMULATIONS

Current research in modeling disproportionately focuses on individual reaction steps, such as adsorbate adsorption, light absorption, or surface reactions. Instead, a coupled microkinetic model is required for a thorough understanding of the process and its improvements. Unfortunately, not many attempts to describe the photoreduction on a microkinetic scale and couple it with CFD have been made. Although they are mostly limited to simple systems, such as CO oxidation, some do study CO_2 photoreduction. Much more common are multiscale efforts on themocatalytic CO_2 reduction.[177,178]

Hammerschmidt et al.[179] studied the CO_2 photoreduction to formic acid on anatase TiO_2 in a multiscale manner. From the Wulff construction, the most prominent facets were discovered to be (101) and (100). To perform kinetic Monte Carlo (kMC) simulations on the (101) surface, thermodynamic parameters (adsorption energies, reaction energies) were procured from the literature and cast into a kMC model. To make the model tractable, several assumptions had to be made (charge transport not considered, holes assumed to react instantaneously, formic acid being the only product). According to the model, inhomogeneous light absorption has an effect on the photocatalytic activity. It was apparent that the illumination intensity and the particle size have a significant impact on the reactivity; namely, smaller particles (40 nm) are efficient but larger particles (145 nm) exhibit higher reactivity.

https://dx.doi.org/10.1021/acscatal.0c02557
ACS Catal. 2020, 10, 14984−15007

Table 3. Overview of Theoretical Studies of Photocatalysts

catalyst	method	excited states	investigated	proposed reaction mechanism	electronic structures calculated	reference
GaP(100)/TiO_2(001)	PBE-GGA	pseudo (emulated with increased H* coverage)	reaction pathway	CO_2 → HCOOH → H_2CO → CH_3OH	orientation relations, DOS, band gap,	128
anatase TiO_2 (101)	PBE-GGA+*U*/HSE	not explicitly	reaction pathway	CO_2→ HCOOH, CO → CH_2O → CH_3OH → CH_3OH → CH_3		173
oxygen vacant				CO_2→ CO → CH_2O → CH_3O →CH_3 → CH_3OH		
anatase TiO_2 (101)	DFT+*U*	not explicitly	reaction pathway	CO_2→ CO → CHO → CHOH → CH_2OH → CH_3OH/CH_4	adsorption energies	132
				CO_2→ CO → CHO → CH_2O → CH_3OH → CH_3OH/CH_4		
Pd/g-C_3N_4	PBE-GGA	not explicitly	reaction pathway	CO_2 → HCOOH → HCHO → CH_3OH → CH_4	adsorption energies	34
Pd/g- C_3N_4	PBE-GGA+ Grimme D3	not explicitly	reaction pathway	CO_2 → HCOO → HCOOH → HCO → CH_2O → CH_2OH → CH_3OH	band gap,	38
Pt/g- C_3N_4				CO_2 → HCOO → HCOOH → HCO → CH_2O → CH_2OH → CH_2 → CH_3 → CH_4	adsorption energies,	
g- C_3N_4					CBM/VBM	
g- C_3N_4	PBE-GGA	no	reaction pathway	CO_2 → HCO_3, HCOOH, CO	HOMO/LUMO,	126
1%KBH- C_3N_4				CO → C→ CH → CH_2 → CH_3 → CH_4	band gap	
2%KBH- C_3N_4						
3%KBH- C_3N_4						
5%KBH- C_3N_4						
Ag_3PO_4(111)/g- C_3N_4	PBE-GGA +Grimme D3	not explicitly	reaction pathway	CO_2 → HCOO → t,c-COOH → HCOOH → HCO → t, c-HCOH → CH_2O → CH_2OH → CH_2 → CH_3 → CH_4	adsorption energies, DOS, charge density differences	45
				CO_2 → t,c-COOH → tt-HOCOH → COH → t-HCOH → CH_2O → CH_2 → CH_3 → CH_4		
g- C_3N_4	PBE-GGA+ GrimmeD3	not explicitly	reaction pathway	CO_2 → HCOO → HCOOH	adsorption energies,	21
Fe/g- C_3N_4					DOS,	
Co/g- C_3N_4					Bader charge analysis	
Cu/g- C_3N_4						
Ni/g- C_3N_4						
g- C_3N_4	PBE-GGA+ GrimmeD3	not explicitly	reaction pathway	CO_2 → HOCO → CO → HCO → H_2CO → CH_3O → CH_3OH	DOS, reductant environment, electron localization function	172
B_4C_3	PBE-GGA + Grimme correction	not explicitly	reaction pathway	CO_2 → HCOO → HCO → CHOH → CH_2OH → CH_2 → CH_3 → CH_4	HOMO/LUMO, band gap, thermodynamic stability, adsorption, CBM/VBM, Carrier mobilities, charge density differences	127
B_{80} fullerene	PBE-GGA + Grimme D2	no	reaction pathway	CO_2→ HOCO → HCOOH	Charge difference diagram, adsorption energies	137
ZnO NSs	PBE-GGA + GrimmeD2	not explicitly	reaction pathway	CO_2 → H_2COOH → H_2CO → H_3COH → H_4COH → CH_4	adsorption energies,	170
Au/ZnO NSs						
Ag/ZnO NSs				CO_2 → H_3COOH → H_3CO → H_3COH → H_4COH → CH_4	charge density difference	
Pd/ZnO NSs						
In_2O_3	B3LYP	LR-TDDFT	absorption spectra	CO_2+H_2 → CO+ H_2O	HOMO/LUMO, absorption spectra,	176
In_2O_{3-x}						
$In_2O_3(OH)_y$						
$In_2O_{3-x}(OH)_y$					charge transfer	

https://dx.doi.org/10.1021/acscatal.0c02557
ACS Catal. 2020, 10, 14984−15007

Few attempts have dealt with the scale-up of the CO_2 photoreduction, mostly due to low conversions and economic viability at present prices. In a study by Chueh et al.,[180] a solar-driven CO_2 reduction in a solar cavity-receiver reactor was investigated. However, the governing mechanism of the reaction was a thermocatalytic conversion with solar energy heating. The cerium oxide catalyst displayed stability and high activity over 500 cycles. The efficiency and the cycling rates were mostly limited by thermal losses (conduction, radiation). A realistic application of such a system is feasible because of the low cost of the cerium oxide catalyst and its longevity (exceeding 500 cycles).

CO oxidation is a more commonly studied reaction due its simplicity. As shown by Matera et. al in a treatment of a *thermo*catalytic reaction, it is possible to link a first-principle kinetic Monte Carlo model (with DFT-supplied data) with computational fluid dynamics.[181,182]

While the theoretical description of the photoreduction itself, combined with the quest for better catalytic materials, has garnered a lot of attention, the other side of the process has remained largely overlooked. The efficiency can be greatly increased with an engineering approach and designing better photoreactor systems. The efficiency is governed by the number of phases involved (gas−solid, gas−liquid−solid), mode of operation (batch, continuous), and catalyst bed (fixed, fluidized).

In addition to ab initio methods and catalyst development, the design and optimization of reactors for the photocatalytic CO_2 reduction is of crucial importance. The reactors can be classified based on the phases involved (two- or three-phase systems) and mode of operation into three categories: slurry, fixed bed, and membrane reactors. Slurry reactors utilize a high surface area but mass transfer limitations, low light utilization, and postprocess separation often make them uneconomical. Fixed-bed reactors offer high conversion rates, low pressure drops, and no cost of separation of the catalyst from the products, but the utilization of photons and coating of the catalyst on the bed surface is problematic. Membrane photoreactors, although exhibiting high yields and selectivities, suffer from low efficiency due to the limited mobility of the charge carriers, as well as mass transfer limitations. For more information, the reader is referred to the review by Khan et al.[121]

For a complete description of the macro scale, mass and heat transfer has to be taken into account. Braham et al.[183] used CFD to study a fluidized bed photoreactor in a complete multiscale simulation using integrated particle, fluid and photo behavior models. The results show that fluidized bed photoreactors should either have very narrow, dense particle beds and small reaction volumes, or larger reaction volumes with a more distributed solids phase. A novel photon absorption behavior was discovered.

A different study in a twin bubbling reactor for CO_2 photoreduction was performed by Chu et al.[184] They made several assumptions regarding the reaction and transport phenomena for the purpose of simplicity (e.g., the photocatalytic reaction rate is only a function of time and not position in the reactor, the gas phase is considered an ideal gas, and the density is a constant). Such assumptions might introduce some discrepancies because light distribution in the reactor is not homogeneous, but rather light dispersion can cause heterogeneities in the reactor, making the position of the particles in the reactor crucial.[183,185,186] The CFD simulations demonstrated that the bubbling twin reactor outperforms the traditional twin reactor in mass transfer, as well as production. Increasing the inlet velocity also shows an increase in the methanol production due to an increased interface area, enhancing mass transfer between the gas and liquid phase.

CO_2 might also be reduced to multicarbon products (C_2, C_3). Although their economic value far surpass C_1 products, the substantial drawback in their production is a comparatively low efficiency/yield. While outside of scope for this work, a recent review by Du et al.[187] discusses recent progress in the field of photocatalytic and electrocatalytic reduction of CO_2 to hydrocarbons. Cu-based catalysts are most often used, but recently, MoS_2 and metallic Pd with boron doping were also probed.

Multiscale models are far and few between. The reasons, although not clearly stated, most likely lie in the complexity of a photocatalytic reaction. While the properties of photocatalysts and their interaction with reactants can be calculated with great accuracy, most studies forego the treatment of excited states and solvent effects due the computational cost involved. This means that the mechanism is only approximately known. The barriers are essentially those of thermocatalytic reduction, making coupling of first-principle calculations with microkinetic models and kMC simulations moot. A successful coupling of DFT with kMC[188,189] and microkinetics[190,191] has already been observed in other fields, whereas photocatalytic CO_2 reduction remains largely underutilized. The next rung on the multiscale ladder, a successful coupling of kMC and microkinetics with CFD, has also been performed.[181,192] An overarching model, encompassing all levels, remains to be realized.

8. CONCLUSIONS

Photocatalysis is increasingly becoming an important alternative for reducing CO_2 emissions. While harboring the potential for a cheaper and environmentally friendlier way of converting CO_2 than the traditional catalytic approaches, it has yet to manifest its full potential. While experimental data are abundant, the theoretical investigations remain limited, mostly focusing on describing one material or used supplementarily to experimental results. Broad screening campaigns, comparative analyses, or exhaustive mechanism treatments are lacking.

Nonetheless, in recent years, theoretical studies have begun to take off. The recent advances in the available computational power have caused the number of purely theoretical studies to surge. Some studies are contrasted with experiments, especially in terms of electronic properties such as CB, VB, band gap, charge transfer, and charge separation calculations. In this Review, we focused on the theoretical description of the CO_2 photoreduction and evaluated the current methodology and trends.

Despite a plethora of the theoretical methods available, density functional theory calculations in a plane-wave approach are most commonly used. GGA approaches are most commonly used for initial calculations, but are being increasingly supplemented with hybrid functionals (such as HSE06 or PBE0), often as single-point calculations. When GGA (most often PBE) is used, a van der Waals correction by Grimme (D2 or D3) are almost universally applied, while the less popular Tkatchenko and Scheffler method also occasionally pops up. When hybrid functional calculations are not desired because of computational cost, the DFT+*U* approach is used as a surrogate. This method, albeit no more computa-

https://dx.doi.org/10.1021/acscatal.0c02557
ACS Catal. 2020, 10, 14984−15007

tionally expensive as GGA, suffers from the inherent untransferability of the *U* parameter, which has to be set for every system, usually by fitting to experimental data. PBE0 and HSE06 are technically not truly ab initio, as the mixing parameter was chosen arbitrarily (by fitting), yet have proved to be a good choice for periodic insulating systems (such as TiO_2). Because of its limitations, B3LYP is more suitable for molecular systems, whereas PBE0 and HSE06 are commonly employed for periodic structures.

Regarding kinetic modeling and macro-scale simulations of photocatalysis, this field is still in its infancy and mostly applied to the thermocatalytic CO_2 reduction due to its simpler nature compared to the photocatalytic reduction. Simplifications have to be made to perform multiscale modeling. At the electronic level, solvent effects and excited states are among the more important aspects, yet most studies ignore them completely. Coupling these results with kMC or microkinetics is a starting point for multiscale models and can subsequently be used as boundary conditions in CFD simulations. There have been studies such as that of Braham et al.[183] that coupled kMC with CFD for photocatalytic system, where the kMC input was derived from first-principles calculations. However, such studies are rarely applied to realistic photocatalytic systems.

In most cases, TiO_2 and g-C_3N_4 stand out as the catalysts of choice. As they are photocatalytically active on their own, their modifications are a promising approach to utilizing them in CO_2 reduction. While photocatalysts with wide band gaps absorb UV light, it is desirable to identify those that can utilize lower frequencies, as well (visible spectrum). This can be achieved with doping, defects (such as oxygen vacancies), cocatalysts, or by employing the Z-scheme type. Nevertheless, the effect of these modifications has to be critically evaluated, as some might act as recombination centers, thus hindering the photocatalytic activity, while others have a positive effect.

Suitable photocatalysts should activate the CO_2 molecule, which is rather inert. Upon adsorption, the C−O bond is elongated, and the molecule is bent, as CO_2^- is formed. Defects and cocatalysts generally improve the activation of the molecule and act as electron sinks. Another important aspect of the catalyst is the exposed surface, as different surfaces exhibit different affinities toward CO_2 and consequently also the intermediates and products. Theoretical studies can screen and thus predict the most suitable surfaces for a desired pathway; therefore, combining theoretical results with surface engineering is a promising new field.

The most common products of CO_2 photoreduction are CO, methanol, and methane, although formaldehyde, formic acid, and hydrocarbons can also form. Simulations show that most suitable photocatalysts exhibit low band-gaps (visible light spectrum absorption), high charge transfer, and good charge separations. While pristine catalysts (e.g., TiO_2 and g-C_3N_4) have good properties, they also possess deficiencies such as a high band gap and a high recombination rate for TiO_2 and g-C_3N_4 respectively. To improve on them, one can resort to defects integration (doping/oxygen vacancies), cocatalysts (electron traps), or a synergistic system of combining two catalysts as in the Z-scheme catalyst. The current trends seem to follow these guidelines, doping the studied material, depositing one or several cocatalysts (usually (noble) metals)), incorporation of oxygen vacancies, or any possible combination, while some investigations are starting to shift their focus toward identification of novel photocatalysts (e.g., B_4C_3).

It is difficult to computationally predict the reaction products as one has to investigate all possible reaction pathways. Nonetheless, theoretical insights can provide important clues and often achieve good agreement with experiments. Methane and methanol are the most prominent products, with a possibility of CO and HCOOH depending on the modifications. While pristine g-C_3N_4 most likely favors methanol and methane production, modifications such as codoping can shift that selectivity toward methane via the carbene pathway. Metal cocatalysts mostly prefer the formation of methane, methanol, or fomaldehyde. Most reactions proceed via HCOOH, while the carbene pathway yields methane. Different modifications can also shift CBM/VBM to the formation of a certain product, while doping and cocatalysts can introduce midgap states. This can either benefit the photocatalysis with a better charge separation or harm it as recombination centers.

Although the theoretical methods for describing the interaction of photons with matter as applied in photocatalysis are getting mature, there is still room for improvement. More costly methods are still not used on larger systems due to their computational cost. Most theoretical work is done without accounting for excited states and solvent effects, while some investigations are starting to take them into account. Despite their known shortcomings, GGA pseudopotentials with simple van der Waals corrections are the predominant approach. In the future, larger screening campaigns will allow for a systematic approach toward photocatalyst improvement and discovery. Moreover, the integration of electronic structure calculations into higher scale simulations (kinetics, computational fluid dynamics, etc.) will result in multiscale models, encompassing all reaction scales from the atomistic to macroscopic level.

AUTHOR INFORMATION

Corresponding Authors

Blaž Likozar − *National Institute of Chemistry, Department of Chemical Reaction Engineering, SI-1001 Ljubljana, Slovenia;* orcid.org/0000-0001-7226-4302; Email: blaz.likozar@ki.si

Matej Huš − *National Institute of Chemistry, Department of Chemical Reaction Engineering, SI-1001 Ljubljana, Slovenia; Association for Technical Culture of Slovenia (ZOTKS), SI-1000 Ljubljana, Slovenia;* orcid.org/0000-0002-8318-5121; Email: matej.hus@ki.si

Author

Žan Kovačič − *National Institute of Chemistry, Department of Chemical Reaction Engineering, SI-1001 Ljubljana, Slovenia*

Complete contact information is available at: https://pubs.acs.org/10.1021/acscatal.0c02557

Notes

The authors declare no competing financial interest.

ACKNOWLEDGMENTS

The authors would like to thank the Slovenian Research Agency fur funding (Core Grant P2-0152 and Grant N2-0135). Ž.K. appreciates the financial support from the European Commission through a Horizon 2020 Project (ReaxPro, Grant N. 814416). M.H. also acknowledges the Slovenian Research Agency for Infrastructure Grant I0-0039.

https://dx.doi.org/10.1021/acscatal.0c02557
ACS Catal. 2020, 10, 14984−15007

We thank Dr Andraž Pavlišič for designing the graphical abstract.

REFERENCES

(1) Goeppert, A.; Czaun, M.; Jones, J. P.; Prakash, S. G. K.; Olah, G. A. Recycling of Carbon Dioxide to Methanol and Derived Products - Closing the Loop. *Chem. Soc. Rev.* **2014**, *43*, 7957−8194.
(2) Xie, S.; Zhang, Q.; Liu, G.; Wang, Y. Photocatalytic and Photoelectrocatalytic Reduction of CO2 Using Heterogeneous Catalysts with Controlled Nanostructures. *Chem. Commun.* **2016**, *52*, 35−59.
(3) Tanaka, K.; Ooyama, D. Multi-Electron Reduction of CO2 via Ru-CO2, -C(O)OH, -CO, -CHO, and -CH2OH Species. *Coord. Chem. Rev.* **2002**, *226*, 211−218.
(4) Koppenol, W. H.; Rush, J. D. Reduction Potential of the Carbon Dioxide/Carbon Dioxide Radical Anion: A Comparison with Other C1 Radicals. *J. Phys. Chem.* **1987**, *91*, 4429−4430.
(5) Nie, X.; Jiang, X.; Wang, H.; Luo, W.; Janik, M. J.; Chen, Y.; Guo, X.; Song, C. Mechanistic Understanding of Alloy Effect and Water Promotion for Pd-Cu Bimetallic Catalysts in CO2 Hydrogenation to Methanol. *ACS Catal.* **2018**, *8*, 4873−4892.
(6) Chu, S.; Ou, P.; Ghamari, P.; Vanka, S.; Zhou, B.; Shih, I.; Song, J.; Mi, Z. Photoelectrochemical CO 2 Reduction into Syngas with the Metal/Oxide Interface. *J. Am. Chem. Soc.* **2018**, *140*, 7869−7877.
(7) Albero, J.; Peng, Y.; García, H. Photocatalytic CO2Reduction to C2+ Products. *ACS Catal.* **2020**, *10*, 5734−5749.
(8) Nie, X.; Esopi, M. R.; Janik, M. J.; Asthagiri, A. Selectivity of CO 2 Reduction on Copper Electrodes: The Role of the Kinetics of Elementary Steps. *Angew. Chem.* **2013**, *125*, 2519−2522.
(9) Liu, S.; Tao, H.; Zeng, L.; Liu, Q.; Xu, Z.; Liu, Q.; Luo, J. L. Shape-Dependent Electrocatalytic Reduction of CO2 to CO on Triangular Silver Nanoplates. *J. Am. Chem. Soc.* **2017**, *139*, 2160−2163.
(10) Gattrell, M.; Gupta, N.; Co, A. A Review of the Aqueous Electrochemical Reduction of CO2 to Hydrocarbons at Copper. *J. Electroanal. Chem.* **2006**, *594*, 1−19.
(11) Xu, H.; Ouyang, S.; Li, P.; Kako, T.; Ye, J. High-Active Anatase TiO2 Nanosheets Exposed with 95% {100} Facets toward Efficient H2 Evolution and CO2 Photoreduction. *ACS Appl. Mater. Interfaces* **2013**, *5*, 1348−1354.
(12) Liu, L.; Jiang, Y.; Zhao, H.; Chen, J.; Cheng, J.; Yang, K.; Li, Y. Engineering Coexposed {001} and {101} Facets in Oxygen-Deficient TiO2 Nanocrystals for Enhanced CO2 Photoreduction under Visible Light. *ACS Catal.* **2016**, *6*, 1097−1108.
(13) Pipornpong, W.; Wanbayor, R.; Ruangpornvisuti, V. Adsorption CO 2 on the Perfect and Oxygen Vacancy Defect Surfaces of Anatase TiO 2 and Its Photocatalytic Mechanism of Conversion to CO. *Appl. Surf. Sci.* **2011**, *257*, 10322−10328.
(14) Teramura, K.; Tanaka, T.; Ishikawa, H.; Kohno, Y.; Funabiki, T. Photocatalytic Reduction of CO2 to CO in the Presence of H2 or CH4 as a Reductant over MgO. *J. Phys. Chem. B* **2004**, *108*, 346−354.
(15) Kohno, Y.; Ishikawa, H.; Tanaka, T.; Funabiki, T.; Yoshida, S. Photoreduction of Carbon Dioxide by Hydrogen over Magnesium Oxide. *Phys. Chem. Chem. Phys.* **2001**, *3*, 1108−1113.
(16) Teramura, K.; Tsuneoka, H.; Shishido, T.; Tanaka, T. Effect of H2 Gas as a Reductant on Photoreduction of CO2 over a Ga2O3 Photocatalyst. *Chem. Phys. Lett.* **2008**, *467*, 191−194.
(17) Di, J.; Zhao, X.; Lian, C.; Ji, M.; Xia, J.; Xiong, J.; Zhou, W.; Cao, X.; She, Y.; Liu, H.; Loh, K. P.; Pennycook, S. J.; Li, H.; Liu, Z. Atomically-Thin Bi 2 MoO 6 Nanosheets with Vacancy Pairs for Improved Photocatalytic CO 2 Reduction. *Nano Energy* **2019**, *61*, 54−59.
(18) Ghuman, K. K.; Wood, T. E.; Hoch, L. B.; Mims, C. A.; Ozin, G. A.; Singh, C. V. Illuminating CO2 Reduction on Frustrated Lewis Pair Surfaces: Investigating the Role of Surface Hydroxides and Oxygen Vacancies on Nanocrystalline In2O3-x(OH)Y. *Phys. Chem. Chem. Phys.* **2015**, *17*, 14623−14635.
(19) Akimov, A. V.; Asahi, R.; Jinnouchi, R.; Prezhdo, O. V. What Makes the Photocatalytic CO2 Reduction on N-Doped Ta2O5 Efficient: Insights from Nonadiabatic Molecular Dynamics. *J. Am. Chem. Soc.* **2015**, *137*, 11517−11525.
(20) Tseng, I. H.; Wu, J. C. S.; Chou, H. Y. Effects of Sol-Gel Procedures on the Photocatalysis of Cu/TiO2 in CO2 Photoreduction. *J. Catal.* **2004**, *221*, 432−440.
(21) Homlamai, K.; Maihom, T.; Choomwattana, S.; Sawangphruk, M.; Limtrakul, J. Single-Atoms Supported (Fe, Co, Ni, Cu) on Graphitic Carbon Nitride for CO2 Adsorption and Hydrogenation to Formic Acid: First-Principles Insights. *Appl. Surf. Sci.* **2020**, *499*, 143928.
(22) Avanesian, T.; Gusmão, G. S.; Christopher, P. Mechanism of CO2 Reduction by H2 on Ru(0 0 0 1) and General Selectivity Descriptors for Late-Transition Metal Catalysts. *J. Catal.* **2016**, *343*, 86−96.
(23) Jia, J.; Wang, H.; Lu, Z.; O'Brien, P. G.; Ghoussoub, M.; Duchesne, P.; Zheng, Z.; Li, P.; Qiao, Q.; Wang, L.; Gu, A.; Jelle, A. A.; Dong, Y.; Wang, Q.; Ghuman, K. K.; Wood, T.; Qian, C.; Shao, Y.; Qiu, C.; Ye, M.; Zhu, Y.; Lu, Z. H.; Zhang, P.; Helmy, A. S.; Singh, C. V.; Kherani, N. P.; Perovic, D. D.; Ozin, G. A. Photothermal Catalyst Engineering: Hydrogenation of Gaseous CO 2 with High Activity and Tailored Selectivity. *Adv. Sci.* **2017**, *4*, 1700252.
(24) Yu, B.; Zhou, Y.; Li, P.; Tu, W.; Li, P.; Tang, L.; Ye, J.; Zou, Z. Photocatalytic Reduction of CO2 over Ag/TiO2 Nanocomposites Prepared with a Simple and Rapid Silver Mirror Method. *Nanoscale* **2016**, *8*, 11870−11874.
(25) Wang, C.; Thompson, R. L.; Baltrus, J.; Matranga, C. Visible Light Photoreduction of CO2 Using CdSe/Pt/TiO2 Heterostructured Catalysts. *J. Phys. Chem. Lett.* **2010**, *1*, 48−53.
(26) Dai, W.; Hu, X.; Wang, T.; Xiong, W.; Luo, X.; Zou, J. Hierarchical CeO 2 /Bi 2 MoO 6 Heterostructured Nanocomposites for Photoreduction of CO 2 into Hydrocarbons under Visible Light Irradiation. *Appl. Surf. Sci.* **2018**, *434*, 481−491.
(27) Li, H.; Wu, X.; Wang, J.; Gao, Y.; Li, L.; Shih, K. Enhanced Activity of Ag-MgO-TiO 2 Catalyst for Photocatalytic Conversion of CO 2 and H 2 O into CH 4. *Int. J. Hydrogen Energy* **2016**, *41*, 8479−8488.
(28) Shi, H.; Zhang, C.; Zhou, C.; Chen, G. Selective Reduction of CO 2 to CO under Visible Light by Controlling Coordination Structures of CeO x -S/ZnIn 2 S 4 Hybrid Catalysts. *RSC Adv.* **2015**, *5*, 93615−93622.
(29) Yang, S.; Gong, Y.; Zhang, J.; Zhan, L.; Ma, L.; Fang, Z.; Vajtai, R.; Wang, X.; Ajayan, P. M. Exfoliated Graphitic Carbon Nitride Nanosheets as Efficient Catalysts for Hydrogen Evolution under Visible Light. *Adv. Mater.* **2013**, *25*, 2452−2456.
(30) Shi, H.; Zhang, C.; Zhou, C.; Chen, G. Conversion of CO2 into Renewable Fuel over Pt-g-C3N4/KNbO3 Composite Photocatalyst. *RSC Adv.* **2015**, *5*, 93615−93622.
(31) Wang, K.; Li, Q.; Liu, B.; Cheng, B.; Ho, W.; Yu, J. Sulfur-Doped g-C3N4 with Enhanced Photocatalytic CO2-Reduction Performance. *Appl. Catal., B* **2015**, *176−177*, 44−52.
(32) Li, X.; Zhuang, Z.; Li, W.; Pan, H. Photocatalytic Reduction of CO2over Noble Metal-Loaded and Nitrogen-Doped Mesoporous TiO2. *Appl. Catal., A* **2012**, *429−430*, 31−38.
(33) Ma, X.; Wu, Y.; Lu, Y.; Xu, J.; Wang, Y.; Zhu, Y. Effect of Compensated Codoping on the Photoelectrochemical Properties of Anatase TiO2 Photocatalyst. *J. Phys. Chem. C* **2011**, *115*, 16963−16969.
(34) Cao, S.; Li, Y.; Zhu, B.; Jaroniec, M.; Yu, J. Facet Effect of Pd Cocatalyst on Photocatalytic CO2 Reduction over G-C3N4. *J. Catal.* **2017**, *349*, 208−217.
(35) Subramanian, V.; Wolf, E. E.; Kamat, P. V. Catalysis with TiO2/Gold Nanocomposites. Effect of Metal Particle Size on the Fermi Level Equilibration. *J. Am. Chem. Soc.* **2004**, *126*, 4943−4950.
(36) Meng, L.; Chen, Z.; Ma, Z.; He, S.; Hou, Y.; Li, H. H.; Yuan, R.; Huang, X. H.; Wang, X.; Wang, X.; Long, J. Gold Plasmon-Induced Photocatalytic Dehydrogenative Coupling of Methane to Ethane on Polar Oxide Surfaces. *Energy Environ. Sci.* **2018**, *11*, 294−298.

https://dx.doi.org/10.1021/acscatal.0c02557
ACS Catal. 2020, 10, 14984−15007

(37) Tan, T. T. Y.; Yip, C. K.; Beydoun, D.; Amal, R. Effects of Nano-Ag Particles Loading on TiO 2 Photocatalytic Reduction of Selenate Ions. *Chem. Eng. J.* **2003**, *95*, 179−186.
(38) Gao, G.; Jiao, Y.; Waclawik, E. R.; Du, A. Single Atom (Pd/Pt) Supported on Graphitic Carbon Nitride as an Efficient Photocatalyst for Visible-Light Reduction of Carbon Dioxide. *J. Am. Chem. Soc.* **2016**, *138*, 6292−6297.
(39) Xu, Q.; Zhang, L.; Yu, J.; Wageh, S.; Al-Ghamdi, A. A.; Jaroniec, M. Direct Z-Scheme Photocatalysts: Principles, Synthesis, and Applications. *Mater. Today* **2018**, *21*, 1042−1063.
(40) Wang, Y.; Shang, X.; Shen, J.; Zhang, Z.; Wu, J. C. S.; Fu, X.; Wang, X.; Li, C.; Wang, D.; Lin, J. Direct and Indirect Z-Scheme Heterostructure-Coupled Photosystem Enabling Cooperation of CO2 Reduction and H2O Oxidation. *Nat. Commun.* **2020**, *11*, 3043.
(41) Di, T.; Zhu, B.; Cheng, B.; Yu, J.; Xu, J. A Direct Z-Scheme g-C3N4/SnS2 Photocatalyst with Superior Visible-Light CO2 Reduction Performance. *J. Catal.* **2017**, *352*, 532−541.
(42) Yuan, Q.; Liu, D.; Zhang, N.; Ye, W.; Ju, H.; Shi, L.; Long, R.; Zhu, J.; Xiong, Y. Noble-Metal-Free Janus-like Structures by Cation Exchange for Z-Scheme Photocatalytic Water Splitting under Broadband Light Irradiation. *Angew. Chem., Int. Ed.* **2017**, *56*, 4206−4210.
(43) Zhu, B.; Xia, P.; Li, Y.; Ho, W.; Yu, J. Fabrication and Photocatalytic Activity Enhanced Mechanism of Direct Z-Scheme g-C 3 N 4 /Ag 2 WO 4 Photocatalyst. *Appl. Surf. Sci.* **2017**, *391*, 175−183.
(44) Li, P.; Zhou, Y.; Li, H.; Xu, Q.; Meng, X.; Wang, X.; Xiao, M.; Zou, Z. All-Solid-State Z-Scheme System Arrays of Fe2V4O13/RGO/CdS for Visible Light-Driving Photocatalytic CO2 Reduction into Renewable Hydrocarbon Fuel. *Chem. Commun.* **2015**, *51*, 800−803.
(45) Tafreshi, S. S.; Moshfegh, A. Z.; De Leeuw, N. H. Mechanism of Photocatalytic Reduction of CO2 by Ag3PO4(111)/g-C3N4 Nanocomposite: A First-Principles Study. *J. Phys. Chem. C* **2019**, *123*, 22191−22201.
(46) Yao, W.; Zhang, B.; Huang, C.; Ma, C.; Song, X.; Xu, Q. Synthesis and Characterization of High Efficiency and Stable Ag 3PO 4/TiO 2 Visible Light Photocatalyst for the Degradation of Methylene Blue and Rhodamine B Solutions. *J. Mater. Chem.* **2012**, *22*, 4050−4055.
(47) Li, F. T.; Zhao, Y.; Wang, Q.; Wang, X. J.; Hao, Y. J.; Liu, R. H.; Zhao, D. Enhanced Visible-Light Photocatalytic Activity of Active Al2O3/g-C3N4 Heterojunctions Synthesized via Surface Hydroxyl Modification. *J. Hazard. Mater.* **2015**, *283*, 371−381.
(48) Wang, J.; Tafen, D. N.; Lewis, J. P.; Hong, Z.; Manivannan, A.; Zhi, M.; Li, M.; Wu, N. Origin of Photocatalytic Activity of Nitrogen-Doped TiO2 Nanobelts. *J. Am. Chem. Soc.* **2009**, *131*, 12290−12297.
(49) Xie, T. H.; Lin, J. Origin of Photocatalytic Deactivation of TiO2 Film Coated on Ceramic Substrate. *J. Phys. Chem. C* **2007**, *111*, 9968−9974.
(50) Jing, L.; Xin, B.; Yuan, F.; Xue, L.; Wang, B.; Fu, H. Effects of Surface Oxygen Vacancies on Photophysical and Photochemical Processes of Zn-Doped TiO2 Nanoparticles and Their Relationships. *J. Phys. Chem. B* **2006**, *110*, 17860−17865.
(51) Wang, G.; Wang, H.; Ling, Y.; Tang, Y.; Yang, X.; Fitzmorris, R. C.; Wang, C.; Zhang, J. Z.; Li, Y. Hydrogen-Treated TiO2 Nanowire Arrays for Photoelectrochemical Water Splitting. *Nano Lett.* **2011**, *11*, 3026−3033.
(52) Zhuang, J.; Dai, W.; Tian, Q.; Li, Z.; Xie, L.; Wang, J.; Liu, P.; Shi, X.; Wang, D. Photocatalytic Degradation of RhB over TiO2 Bilayer Films: Effect of Defects and Their Location. *Langmuir* **2010**, *26*, 9686−9694.
(53) Li, J.; Zhang, M.; Guan, Z.; Li, Q.; He, C.; Yang, J. Synergistic Effect of Surface and Bulk Single-Electron-Trapped Oxygen Vacancy of TiO2 in the Photocatalytic Reduction of CO2. *Appl. Catal., B* **2017**, *206*, 300−307.
(54) Hoch, L. B.; Szymanski, P.; Ghuman, K. K.; Hea, L.; Liao, K.; Qiao, Q.; Reyes, L. M.; Zhu, Y.; El-Sayed, M. A.; Singh, C. V.; Ozin, G. A. Carrier Dynamics and the Role of Surface Defects: Designing a Photocatalyst for Gas-Phase CO2 Reduction. *Proc. Natl. Acad. Sci. U. S. A.* **2016**, *113*, 8011−8020.
(55) Jin, X.; Lv, C.; Zhou, X.; Ye, L.; Xie, H.; Liu, Y.; Su, H.; Zhang, B.; Chen, G. Oxygen Vacancy Engineering of Bi24O31Cl10 for Boosted Photocatalytic CO2 Conversion. *ChemSusChem* **2019**, *12*, 2740−2747.
(56) Neaţu, Ş.; Maciá-Agulló, J. A.; Garcia, H. Solar Light Photocatalytic CO2 Reduction: General Considerations and Selected Bench-Mark Photocatalysts. *Int. J. Mol. Sci.* **2014**, *15*, 5246−5262.
(57) Singh, A. K.; Mathew, K.; Zhuang, H. L.; Hennig, R. G. Computational Screening of 2D Materials for Photocatalysis. *J. Phys. Chem. Lett.* **2015**, *6*, 1087−1098.
(58) Wang, X.; Wang, F.; Sang, Y.; Liu, H. Full-Spectrum Solar-Light-Activated Photocatalysts for Light − Chemical Energy Conversion. *Adv. Energy Mater.* **2017**, *7*, 1700473.
(59) Chen, S.; Huang, D.; Xu, P.; Xue, W.; Lei, L.; Cheng, M.; Wang, R.; Liu, X.; Deng, R. Semiconductor-Based Photocatalysts for Photocatalytic and Photoelectrochemical Water Splitting: Will We Stop with Photocorrosion? *J. Mater. Chem. A* **2020**, *8*, 2286−2322.
(60) Yang, N.; Zhai, J.; Wang, D.; Chen, Y.; Jiang, L. Two-Dimensional Graphene Bridges Enhanced Photoinduced Charge Transport in Dye-Sensitized Solar Cells. *ACS Nano* **2010**, *4*, 887−894.
(61) Mu, L.; Zhao, Y.; Li, A.; Wang, S.; Wang, Z.; Yang, J.; Wang, Y.; Liu, T.; Chen, R.; Zhu, J.; Fan, F.; Li, R.; Li, C. Environmental Science Enhancing Charge Separation on High Symmetry SrTiO 3 Exposed with Anisotropic Facets for Photocatalytic Water Splitting †. *Energy Environ. Sci.* **2016**, *9*, 2463−2469.
(62) Kumar, S. G.; Devi, L. G. *J. Phys. Chem. A* **2011**, *115*, 13211−13241.
(63) Weng, B.; Qi, M. Y.; Han, C.; Tang, Z. R.; Xu, Y. J. Photocorrosion Inhibition of Semiconductor-Based Photocatalysts: Basic Principle, Current Development, and Future Perspective. *ACS Catal.* **2019**, *9*, 4642−4687.
(64) Xu, S.; Carter, E. A. Theoretical Insights into Heterogeneous (Photo)Electrochemical CO2 Reduction. *Chem. Rev.* **2019**, *119*, 6631−6669.
(65) Matsubara, Y.; Grills, D. C.; Kuwahara, Y. Thermodynamic Aspects of Electrocatalytic CO2 Reduction in Acetonitrile and with an Ionic Liquid as Solvent or Electrolyte. *ACS Catal.* **2015**, *5*, 6440−6452.
(66) Sato, S.; Morikawa, T.; Saeki, S.; Kajino, T.; Motohiro, T. Visible-Light-Induced Selective CO2 Reduction Utilizing a Ruthenium Complex Electrocatalyst Linked to a p-Type Nitrogen-Doped Ta2O5 Semiconductor. *Angew. Chem., Int. Ed.* **2010**, *49*, 5101−5105.
(67) Li, C.; Xu, Y.; Tu, W.; Chen, G.; Xu, R. Metal-Free Photocatalysts for Various Applications in Energy Conversion and Environmental Purification. *Green Chem.* **2017**, *19*, 882−899.
(68) Liao, P.; Carter, E. A. New Concepts and Modeling Strategies to Design and Evaluate Photo-Electro-Catalysts Based on Transition Metal Oxides. *Chem. Soc. Rev.* **2013**, *42*, 2401−2422.
(69) Shockley, W.; Queisser, H. J. Detailed Balance Limit of Efficiency of P-n Junction Solar Cells. *J. Appl. Phys.* **1961**, *32*, 510−519.
(70) Xu, Y.; Schoonen, M. A. A. The Absolute Energy Positions of Conduction and Valence Bands of Selected Semiconducting Minerals. *Am. Mineral.* **2000**, *85*, 543−556.
(71) Anthony, B. J. E.; Facchetti, A.; Heeney, M.; Marder, S. R.; Zhan, X. N-Type Organic Semiconductors in Organic Electronics. *Adv. Mater.* **2010**, *22*, 3876−3892.
(72) Ghuman, K. K.; Singh, C. V. Effect of Doping on Electronic Structure and Photocatalytic Behavior of Amorphous TiO2. *J. Phys.: Condens. Matter* **2013**, *25*, 475501.
(73) Li, X. Z.; Li, F. B. Study of Au/Au3+-TiO2 Photocatalysts toward Visible Photooxidation for Water and Wastewater Treatment. *Environ. Sci. Technol.* **2001**, *35*, 2381−2387.
(74) Vamathevan, V.; Tse, H.; Amal, R.; Low, G.; McEvoy, S. Effects of Fe3+ and Ag+ Ions on the Photocatalytic Degradation of Sucrose in Water. *Catal. Today* **2001**, *68*, 201−208.

https://dx.doi.org/10.1021/acscatal.0c02557
ACS Catal. 2020, 10, 14984−15007

(75) Maeda, K.; Domen, K. New Non-Oxide Photocatalysts Designed for Overall Water Splitting under Visible Light. *J. Phys. Chem. C* **2007**, *111*, 7851−7861.
(76) Sadeghi, M.; Liu, W.; Zhang, T. G.; Stavropoulos, P.; Levy, B. Role of Photoinduced Charge Carrier Separation Distance in Heterogeneous Photocatalysis: Oxidative Degradation of CH3OH Vapor in Contact with Pt/TiO2 and Cofumed TiO2-Fe2O3. *J. Phys. Chem.* **1996**, *100*, 19466−19474.
(77) Marschall, R.; Wang, L. Non-Metal Doping of Transition Metal Oxides for Visible-Light Photocatalysis. *Catal. Today* **2014**, *225*, 111−135.
(78) Scholes, D. T.; Yee, P. Y.; Lindemuth, J. R.; Kang, H.; Onorato, J.; Ghosh, R.; Luscombe, C. K.; Spano, F. C.; Tolbert, S. H.; Schwartz, B. J. The Effects of Crystallinity on Charge Transport and the Structure of Sequentially Processed F4TCNQ-Doped Conjugated Polymer Films. *Adv. Funct. Mater.* **2017**, *27*, 1−13.
(79) Pan, Y. X.; You, Y.; Xin, S.; Li, Y.; Fu, G.; Cui, Z.; Men, Y. L.; Cao, F. F.; Yu, S. H.; Goodenough, J. B. Photocatalytic CO2 Reduction by Carbon-Coated Indium-Oxide Nanobelts. *J. Am. Chem. Soc.* **2017**, *139*, 4123−4129.
(80) Butburee, T.; Kotchasarn, P.; Hirunsit, P.; Sun, Z.; Tang, Q.; Khemthong, P.; Sangkhun, W.; Thongsuwan, W.; Kumnorkaew, P.; Wang, H.; Faungnawakij, K. New Understanding of Crystal Control and Facet Selectivity of Titanium Dioxide Ruling Photocatalytic Performance. *J. Mater. Chem. A* **2019**, *7*, 8156−8166.
(81) Kou, J.; Lu, C.; Wang, J.; Chen, Y.; Xu, Z.; Varma, R. S. Selectivity Enhancement in Heterogeneous Photocatalytic Transformations. *Chem. Rev.* **2017**, *117*, 1445−1514.
(82) Tu, W.; Guo, W.; Hu, J.; He, H.; Li, H.; Li, Z.; Luo, W.; Zhou, Y.; Zou, Z. State-of-the-Art Advancements of Crystal Facet-Exposed Photocatalysts beyond TiO2: Design and Dependent Performance for Solar Energy Conversion and Environment Applications. *Mater. Today* **2020**, *33*, 75−86.
(83) Hohenberg, P.; Kohn, W. Inhomogeneous Electron Gas. *Phys. Rev.* **1964**, *136*, B864−B871.
(84) Kohn, W.; Sham, L. J. Self-Consistent Equations Including Exchange and Correlation Effects. *Phys. Rev.* **1965**, *140*, A1133−A1138.
(85) Perdew, J. P.; Zunger, A. Self-Interaction Correction to Density-Functional Approximations for Many-Electron Systems. *Phys. Rev. B: Condens. Matter Mater. Phys.* **1981**, *23*, 5048−5079.
(86) Perdew, J. P.; Chevary, J. A.; Vosko, S. H.; Jackson, K. A.; Pederson, M. R.; Singh, D. J.; Fiolhais, C. Atoms, Molecules, Solids, and Surfaces: Applications of the Generalized Gradient Approximation for Exchange and Correlation. *Phys. Rev. B: Condens. Matter Mater. Phys.* **1992**, *46*, 6671−6687.
(87) Becke, A. D. Density-Functional Thermochemistry. III. The Role of Exact Exchange. *J. Chem. Phys.* **1993**, *98*, 5648−5652.
(88) Sim, F.; St. Amant, A.; Papai, I.; Salahub, D. R. Gaussian Density Functional Calculations on Hydrogen-Bonded Systems. *J. Am. Chem. Soc.* **1992**, *114*, 4391−4400.
(89) Hammer, B.; Jacobsen, K. W.; Nørskov, J. K. Role of Nonlocal Exchange Correlation in Activated Adsorption. *Phys. Rev. Lett.* **1993**, *70*, 3971−3974.
(90) Kong, X. J.; CHan, C. T.; Ho, K. M.; Ye, Y. Y. Cohesive Properties of Crystalline Solids by the Generalized Gradient Approximation. *Phys. Rev. B: Condens. Matter Mater. Phys.* **1990**, *42*, 9357−9364.
(91) Mori-Sánchez, P.; Cohen, A. J.; Yang, W. Many-Electron Self-Interaction Error in Approximate Density Functionals. *J. Chem. Phys.* **2006**, *125*, 201102.
(92) Comba, P. *Modeling of Molecular Properties*, 1st ed.; Comba, P., Ed.; Wiley-VCH Verlag GmbH & Co. KGaA: Weinheim, 2011; p 137.
(93) Cohen, A. J.; Mori-Sánchez, P.; Yang, W. Insights into Current Limitations of Density Functional Theory. *Science (Washington, DC, U. S.)* **2008**, *321*, 792−794.
(94) Mori-Sánchez, P.; Cohen, A. J.; Yang, W. Localization and Delocalization Errors in Density Functional Theory and Implications for Band-Gap Prediction. *Phys. Rev. Lett.* **2008**, *100*, 146401.
(95) Morales-García, Á.; Valero, R.; Illas, F. An Empirical, yet Practical Way to Predict the Band Gap in Solids by Using Density Functional Band Structure Calculations. *J. Phys. Chem. C* **2017**, *121*, 18862−18866.
(96) Terakura, K.; Oguchi, T.; Williams, A. R.; Kübler, J. Band Theory of Insulating Transition-Metal Monoxides: Band-Structure Calculations. *Phys. Rev. B: Condens. Matter Mater. Phys.* **1984**, *30*, 4734−4747.
(97) Anisimov, V. I.; Zaanen, J.; Andersen, O. K. Band Theory and Mott Insulators: Hubbard U Instead of Stoner I. *Phys. Rev. B: Condens. Matter Mater. Phys.* **1991**, *44*, 943−954.
(98) Hubbard, J.; A, P. R. S. L. Electron Correlations in Narrow Energy Bands. *Proc. R. Soc. London. Ser. A. Math. Phys. Sci.* **1963**, *276*, 238−257.
(99) Liechtenstein, a. I.; Anisimov, V. I.; Zaanen, J. Density-Functional Theory and Strong Interactions: Orbital Ordering in Mott-Hubbard Insulators. *Phys. Rev. B: Condens. Matter Mater. Phys.* **1995**, *52*, R5467−R5471.
(100) Cinquini, F.; Giordano, L.; Pacchioni, G.; Ferrari, A. M.; Pisani, C.; Roetti, C. Electronic Structure of NiO Ag (100) Thin Films from DFT+U and Hybrid Functional DFT Approaches. *Phys. Rev. B: Condens. Matter Mater. Phys.* **2006**, *74*, 165403.
(101) Verma, P.; Truhlar, D. G. Does DFT+U Mimic Hybrid Density Functionals? *Theor. Chem. Acc.* **2016**, *135*, 182.
(102) Hedin, L. New Method for Calculating the One-Particle Green's Function with Application to the Electron-Gas Problem*. *Phys. Rev.* **1965**, *139*, A796−A823.
(103) Aulbur, W. G.; Jönsson, L.; Wilkins, J. W. Quasiparticle Calculations in Solids. *Solid State Phys.* **2000**, *54*, 1−218.
(104) Tripkovic, V.; Hansen, H. A.; Garcia-Lastra, J. M.; Vegge, T. Comparative DFT+U and HSE Study of the Oxygen Evolution Electrocatalysis on Perovskite Oxides. *J. Phys. Chem. C* **2018**, *122*, 1135−1147.
(105) Paier, J.; Marsman, M.; Hummer, K.; Kresse, G.; Gerber, I. C.; Angyán, J. G. Screened Hybrid Density Functionals Applied to Solids. *J. Chem. Phys.* **2006**, *124*, 154709−154723.
(106) Marques, M. A. L.; Vidal, J.; Oliveira, M. J. T.; Reining, L.; Botti, S. Density-Based Mixing Parameter for Hybrid Functionals. *Phys. Rev. B - Condens. Matter Mater. Phys.* **2011**, *83*, 035119.
(107) Ernzerhof, M.; Scuseria, G. E. Assessment of the Perdew-Burke-Ernzerhof Exchange-Correlation Functional. *J. Chem. Phys.* **1999**, *110*, 5029−5036.
(108) Heyd, J.; Scuseria, G. E. Efficient Hybrid Density Functional Calculations in Solids: Assessment of the Heyd-Scuseria-Ernzerhof Screened Coulomb Hybrid Functional. *J. Chem. Phys.* **2004**, *121*, 1187−1192.
(109) Heyd, J.; Peralta, J. E.; Scuseria, G. E.; Martin, R. L. Energy Band Gaps and Lattice Parameters Evaluated with the Heyd-Scuseria-Ernzerhof Screened Hybrid Functional. *J. Chem. Phys.* **2005**, *123*, 174101.
(110) Vydrov, O. A.; Heyd, J.; Krukau, A. V.; Scuseria, G. E. Importance of Short-Range versus Long-Range Hartree-Fock Exchange for the Performance of Hybrid Density Functionals. *J. Chem. Phys.* **2006**, *125*, 074106.
(111) Lee, C.; Yang, W.; Parr, R. Development of the Colic-Salvetti Correlation-Energy Formula into a Functional of the Electron Density. *Phys. Rev. B: Condens. Matter Mater. Phys.* **1988**, *37*, 785−789.
(112) Paier, J.; Marsman, M.; Kresse, G. Why Does the B3LYP Hybrid Functional Fail for Metals? *J. Chem. Phys.* **2007**, *127*, 024103.
(113) Feng, X. Electronic Structure of MnO and CoO from File B3LYP Hybrid Density Functional Method. *Phys. Rev. B - Condens. Matter Mater. Phys.* **2004**, *69*, 155107.
(114) Feng, X. Electronic Structures and Ferromagnetism of Cu- and Mn-Doped ZnO. *J. Phys.: Condens. Matter* **2004**, *16*, 4251−4259.

https://dx.doi.org/10.1021/acscatal.0c02557
ACS Catal. 2020, 10, 14984−15007

(115) Loschen, C.; Carrasco, J.; Neyman, K. M.; Illas, F. First-Principles LDA+U and GGA+U Study of Cerium Oxides: Dependence on the Effective U Parameter. *Phys. Rev. B - Condens. Matter Mater. Phys.* **2007**, *75*, 035115.
(116) Hybertsen, M. S.; Louie, S. G. Electron Correlation in Semiconductors and Insulators: Band Gaps and Quasiparticle Energies. *Phys. Rev. B: Condens. Matter Mater. Phys.* **1986**, *34*, 5390−5413.
(117) Salpeter, E. E.; Bethe, H. A. A Relativistic Equation for Bound-State Problems. *Phys. Rev.* **1951**, *84*, 1232−1242.
(118) Perdew, J. P.; Burke, K.; Ernzerhof, M. Generalized Gradient Approximation Made Simple. *Phys. Rev. Lett.* **1996**, *77*, 3865−3868.
(119) Amaya-Roncancio, S.; Arroyo-Gómez, J. J.; Linares, D. H.; Sapag, K. Direct versus Hydrogen-Assisted Dissociation of CO on Iron Surfaces: Kinetic Monte Carlo and Microkinetic Modeling. *J. Mol. Struct.* **2020**, *1201*, 127188.
(120) Andersen, M.; Plaisance, C. P.; Reuter, K. Assessment of Mean-Field Microkinetic Models for CO Methanation on Stepped Metal Surfaces Using Accelerated Kinetic Monte Carlo. *J. Chem. Phys.* **2017**, *147*, 152705.
(121) Khan, A. A.; Tahir, M. Recent Advancements in Engineering Approach towards Design of Photo-Reactors for Selective Photocatalytic CO2 Reduction to Renewable Fuels. *J. CO2 Util.* **2019**, *29*, 205−239.
(122) Choi, W.; Termin, A.; Hoffmann, M. R. The Role of Metal Ion Dopants in Quantum-Sized TiO2: Correlation between Photoreactivity and Charge Carrier Recombination Dynamics. *J. Phys. Chem.* **1994**, *98*, 13669−13679.
(123) Chen, C.; Ma, W.; Zhao, J. Photocatalytic Degradation of Organic Pollutants by Co-Doped TiO2 Under Visible Light Irradiation. *Curr. Org. Chem.* **2010**, *14*, 630−644.
(124) Liu, L.; Fan, W.; Zhao, X.; Sun, H.; Li, P.; Sun, L. Surface Dependence of CO2 Adsorption on Zn2GeO4. *Langmuir* **2012**, *28*, 10415−10424.
(125) Hahn, K. R.; Iannuzzi, M.; Seitsonen, A. P.; Hutter, J. Coverage Effect of the CO2 Adsorption Mechanisms on CeO 2(111) by First Principles Analysis. *J. Phys. Chem. C* **2013**, *117*, 1701−1711.
(126) Wang, K.; Fu, J.; Zheng, Y. Insights into Photocatalytic CO2 Reduction on C3N4: Strategy of Simultaneous B, K Co-Doping and Enhancement by N Vacancies. *Appl. Catal., B* **2019**, *254*, 270−282.
(127) Chang, H.; Tu, K.; Zhang, X.; Zhao, J.; Zhou, X.; Zhang, H. B4C3Monolayer with Impressive Electronic, Optical, and Mechanical Properties: A Potential Metal-Free Photocatalyst for CO2 Reduction under Visible Light. *J. Phys. Chem. C* **2019**, *123*, 25091−25101.
(128) Li, L. F.; Li, Y. F.; Liu, Z. P. CO2 Photoreduction via Quantum Tunneling: Thin TiO2-Coated GaP with Coherent Interface to Achieve Electron Tunneling. *ACS Catal.* **2019**, *9*, 5668−5678.
(129) Wang, Y.; Tian, Y.; Yan, L.; Su, Z. DFT Study on Sulfur-Doped g - C 3 N 4 Nanosheets as a Photocatalyst for CO 2 Reduction Reaction. *J. Phys. Chem. C* **2018**, *122*, 7712−7719.
(130) He, H.; Zapol, P.; Curtiss, L. A. A Theoretical Study of CO2 Anions on Anatase (101) Surface. *J. Phys. Chem. C* **2010**, *114*, 21474−21481.
(131) Ye, J.; Liu, C.; Ge, Q. DFT Study of CO 2 Adsorption and Hydrogenation on the in 2O 3 Surface. *J. Phys. Chem. C* **2012**, *116*, 7817−7825.
(132) Liu, J. Y.; Gong, X. Q.; Alexandrova, A. N. Mechanism of CO 2 Photocatalytic Reduction to Methane and Methanol on Defected Anatase TiO 2 (101): A Density Functional Theory Study. *J. Phys. Chem. C* **2019**, *123*, 3505−3511.
(133) Hammami, R.; Dhouib, A.; Fernandez, S.; Minot, C. CO2 Adsorption on (0 0 1) Surfaces of Metal Monoxides with Rock-Salt Structure. *Catal. Today* **2008**, *139*, 227−233.
(134) Jensen, M. B.; Pettersson, L. G. M.; Swang, O.; Olsbye, U. CO2 Sorption on MgO and CaO Surfaces: A Comparative Quantum Chemical Cluster Study. *J. Phys. Chem. B* **2005**, *109*, 16774−16781.
(135) Saputro, A. G.; Agusta, M. K.; Wungu, T. D. K.; Suprijadi; Rusydi, F.; Dipojono, H. K. DFT Study of Adsorption of CO2 on Palladium Cluster Doped by Transition Metal. *J. Phys.: Conf. Ser.* **2016**, *739*, 012083.
(136) Zhu, B.; Zhang, L.; Xu, D.; Cheng, B.; Yu, J. Adsorption Investigation of CO2 on G-C3N4 Surface by DFT Calculation. *J. CO2 Util.* **2017**, *21*, 327−335.
(137) Qu, M.; Qin, G.; Du, A.; Fan, J.; Sun, Q. B80 Fullerene: A Promising Metal-Free Photocatalyst for Efficient Conversion of CO2 to HCOOH. *J. Phys. Chem. C* **2019**, *123*, 24193−24199.
(138) Sun, Q.; Wang, M.; Li, Z.; Du, A.; Searles, D. J. Carbon Dioxide Capture and Gas Separation on B 80 Fullerene. *J. Phys. Chem. C* **2014**, *118*, 2170−2177.
(139) Raskó, J.; Solymosi, F. Infrared Spectroscopic Study of the Photoinduced Activation of CO2 on TiO2 and Rh/TiO2 Catalysts. *J. Phys. Chem.* **1994**, *98*, 7147−7152.
(140) Indrakanti, V. P.; Schobert, H. H.; Kubicki, J. D. Quantum Mechanical Modeling of CO 2 Interactions with Irradiated Stoichiometric and Oxygen-Deficient Anatase TiO 2 Surfaces: Implications for the Photocatalytic Reduction of CO 2. *Energy Fuels* **2009**, *23*, 5247−5256.
(141) Jia, L.; Wu, C.; Han, S.; Yao, N.; Li, Y.; Li, Z.; Chi, B.; Pu, J.; Jian, L. Theoretical Study on the Electronic and Optical Properties of (N, Fe)-Codoped Anatase TiO2 Photocatalyst. *J. Alloys Compd.* **2011**, *509*, 6067−6071.
(142) Janotti, A.; Varley, J. B.; Rinke, P.; Umezawa, N.; Kresse, G.; Van De Walle, C. G. Hybrid Functional Studies of the Oxygen Vacancy in TiO2. *Phys. Rev. B: Condens. Matter Mater. Phys.* **2010**, *81*, 085212.
(143) Jin, C.; Dai, Y.; Wei, W.; Ma, X.; Li, M.; Huang, B. Effects of Single Metal Atom (Pt, Pd, Rh and Ru) Adsorption on the Photocatalytic Properties of Anatase TiO 2. *Appl. Surf. Sci.* **2017**, *426*, 639−646.
(144) Liu, J. Origin of High Photocatalytic Efficiency in Monolayer G-C3N4/CdS Heterostructure: A Hybrid DFT Study. *J. Phys. Chem. C* **2015**, *119*, 28417−28423.
(145) Fang, Z.; Weng, S.; Ye, X.; Feng, W.; Zheng, Z.; Lu, M.; Lin, S.; Fu, X.; Liu, P. Defect Engineering and Phase Junction Architecture of Wide-Bandgap ZnS for Conflicting Visible Light Activity in Photocatalytic H2 Evolution. *ACS Appl. Mater. Interfaces* **2015**, *7*, 13915−13924.
(146) Yu, W.; Zhang, J.; Peng, T. New Insight into the Enhanced Photocatalytic Activity of N-, C- and S-Doped ZnO Photocatalysts. *Appl. Catal., B* **2016**, *181*, 220−227.
(147) Li, Q.; Meng, H.; Zhou, P.; Zheng, Y.; Wang, J.; Yu, J.; Gong, J. Zn1- XCdxS Solid Solutions with Controlled Bandgap and Enhanced Visible-Light Photocatalytic H2-Production Activity. *ACS Catal.* **2013**, *3*, 882−889.
(148) Fang, D. Q.; Chen, X.; Gao, P. F.; Zhang, Y.; Zhang, S. L. Mono- and Bilayer ZnSnN2 Sheets for Visible-Light Photocatalysis: First-Principles Predictions. *J. Phys. Chem. C* **2017**, *121*, 26063−26068.
(149) Meng, R.; Sun, X.; Yang, D.; Bao, J.; Chen, X. Two Dimensional XAs (X = Si, Ge, Sn) Monolayers as Promising Photocatalysts for Water Splitting Hydrogen Production with High Carrier Mobility. *Appl. Mater. Today* **2018**, *13*, 276−284.
(150) Lian, X.; Niu, M.; Huang, Y.; Cheng, D. MoS2-CdS Heterojunction with Enhanced Photocatalytic Activity: A First Principles Study. *J. Phys. Chem. Solids* **2018**, *120*, 52−56.
(151) Toroker, M. C.; Kanan, D. K.; Alidoust, N.; Isseroff, L. Y.; Liao, P.; Carter, E. A. First Principles Scheme to Evaluate Band Edge Positions in Potential Transition Metal Oxide Photocatalysts and Photoelectrodes. *Phys. Chem. Chem. Phys.* **2011**, *13*, 16644−16654.
(152) Kanan, D. K.; Carter, E. A. Band Gap Engineering of MnO via ZnO Alloying: A Potential New Visible-Light Photocatalyst. *J. Phys. Chem. C* **2012**, *116*, 9876−9887.
(153) Wang, J.; Yu, Y.; Zhang, L. Highly Efficient Photocatalytic Removal of Sodium Pentachlorophenate with Bi3O4Br under Visible Light. *Appl. Catal., B* **2013**, *136−137*, 112−121.

https://dx.doi.org/10.1021/acscatal.0c02557
ACS Catal. 2020, 10, 14984−15007

(154) Zhuang, H. L.; Hennig, R. G. Theoretical Perspective of Photocatalytic Properties of Single-Layer SnS2. *Phys. Rev. B: Condens. Matter Mater. Phys.* **2013**, *88*, 115314.
(155) Li, X.; Wen, J.; Low, J.; Fang, Y.; Yu, J. Design and Fabrication of Semiconductor Photocatalyst for Photocatalytic Reduction of CO2 to Solar Fuel. *Sci. China Mater.* **2014**, *57*, 70−100.
(156) Tahir, M.; Amin, N. A. S. Indium-Doped TiO2 Nanoparticles for Photocatalytic CO2 Reduction with H2O Vapors to CH4. *Appl. Catal., B* **2015**, *162*, 98−109.
(157) Qin, S.; Xin, F.; Liu, Y.; Yin, X.; Ma, W. Photocatalytic Reduction of CO2 in Methanol to Methyl Formate over CuO-TiO2 Composite Catalysts. *J. Colloid Interface Sci.* **2011**, *356*, 257−261.
(158) Corma, A.; Garcia, H. Photocatalytic Reduction of CO2 for Fuel Production: Possibilities and Challenges. *J. Catal.* **2013**, *308*, 168−175.
(159) Akhter, P.; Hussain, M.; Saracco, G.; Russo, N. Novel Nanostructured-TiO2Materials for the Photocatalytic Reduction of CO2 Greenhouse Gas to Hydrocarbons and Syngas. *Fuel* **2015**, *149*, 55−65.
(160) Baran, T.; Wojtyła, S.; Dibenedetto, A.; Aresta, M.; Macyk, W. Zinc Sulfide Functionalized with Ruthenium Nanoparticles for Photocatalytic Reduction of CO2. *Appl. Catal., B* **2015**, *178*, 170−176.
(161) Lo, C. C.; Hung, C. H.; Yuan, C. S.; Hung, Y. L. Parameter Effects and Reaction Pathways of Photoreduction of CO 2 over TiO 2 /SO 42- Photocatalyst. *Chin. J. Catal.* **2007**, *28*, 528−534.
(162) Tahir, M.; Tahir, B.; Amin, N. A. S. Photocatalytic Reverse Water Gas Shift CO2 Reduction to CO over Montmorillonite Supported TiO2 Nanocomposite. *Chem. Eng. Trans.* **2017**, *56*, 319−324.
(163) Sun, W.; Qian, C.; He, L.; Ghuman, K. K.; Wong, A. P. Y.; Jia, J.; Jelle, A. A.; O'Brien, P. G.; Reyes, L. M.; Wood, T. E.; Helmy, A. S.; Mims, C. A.; Singh, C. V.; Ozin, G. A. Heterogeneous Reduction of Carbon Dioxide by Hydride-Terminated Silicon Nanocrystals. *Nat. Commun.* **2016**, *7*, 12553.
(164) Dong, Y.; Ghuman, K. K.; Popescu, R.; Duchesne, P. N.; Zhou, W.; Loh, J. Y. Y.; Jelle, A. A.; Jia, J.; Wang, D.; Mu, X.; Kübel, C.; Wang, L.; He, L.; Ghoussoub, M.; Wang, Q.; Wood, T. E.; Reyes, L. M.; Zhang, P.; Kherani, N. P.; Singh, C. V.; Ozin, G. A. Solar Fuels: Tailoring Surface Frustrated Lewis Pairs of In2O3−x(OH)y for Gas-Phase Heterogeneous Photocatalytic Reduction of CO2 by Isomorphous Substitution of In3+ with Bi3+. *Adv. Sci.* **2018**, *5*, 1870034.
(165) Xu, F.; Zhang, J.; Zhu, B.; Yu, J.; Xu, J. CuInS 2 Sensitized TiO 2 Hybrid Nanofibers for Improved Photocatalytic CO 2 Reduction. *Appl. Catal., B* **2018**, *230*, 194−202.
(166) Xu, F.; Meng, K.; Zhu, B.; Liu, H.; Xu, J.; Yu, J. Graphdiyne: A New Photocatalytic CO2 Reduction Cocatalyst. *Adv. Funct. Mater.* **2019**, *29*, 1−8.
(167) Ma, Z.; Li, P.; Ye, L.; Wang, L.; Xie, H.; Zhou, Y. Selectivity Reversal of Photocatalytic CO 2 Reduction by Pt Loading. *Catal. Sci. Technol.* **2018**, *8*, 5129−5132.
(168) Tu, W.; Zhou, Y.; Li, H.; Li, P.; Zou, Z. Au@TiO2 Yolk-Shell Hollow Spheres for Plasmon-Induced Photocatalytic Reduction of CO2 to Solar Fuel via a Local Electromagnetic Field. *Nanoscale* **2015**, *7*, 14232−14236.
(169) Huo, Y.; Zhang, J.; Dai, K.; Li, Q.; Lv, J.; Zhu, G.; Liang, C. All-Solid-State Artificial Z-Scheme Porous g-C3N4/Sn2S3-DETA Heterostructure Photocatalyst with Enhanced Performance in Photocatalytic CO2 Reduction. *Appl. Catal., B* **2019**, *241*, 528−538.
(170) Zhao, J.; Liu, B.; Meng, L.; He, S.; Yuan, R.; Hou, Y.; Ding, Z.; Lin, H.; Zhang, Z.; Wang, X.; Long, J. Plasmonic Control of Solar-Driven CO2 Conversion at the Metal/ZnO Interfaces. *Appl. Catal., B* **2019**, *256*, 117823.
(171) Anpo, M.; Yamashita, H.; Ichihashi, Y.; Ehara, S. Photocatalytic Reduction of CO2 with H2O on Various Titanium Oxide Catalysts. *J. Electroanal. Chem.* **1995**, *396*, 21−26.
(172) Azofra, L. M.; MacFarlane, D. R.; Sun, C. A DFT Study of Planar: Vs. Corrugated Graphene-like Carbon Nitride (g-C3N4) and Its Role in the Catalytic Performance of CO2 Conversion. *Phys. Chem. Chem. Phys.* **2016**, *18*, 18507−18514.
(173) Ji, Y.; Luo, Y. New Mechanism for Photocatalytic Reduction of CO2 on the Anatase TiO2(101) Surface: The Essential Role of Oxygen Vacancy. *J. Am. Chem. Soc.* **2016**, *138*, 15896−15902.
(174) Ji, Y.; Luo, Y. Theoretical Study on the Mechanism of Photoreduction of CO2 to CH4 on the Anatase TiO2(101) Surface. *ACS Catal.* **2016**, *6*, 2018−2025.
(175) Karamian, E.; Sharifnia, S. On the General Mechanism of Photocatalytic Reduction of CO2. *J. CO2 Util.* **2016**, *16*, 194−203.
(176) Ghuman, K. K.; Hoch, L. B.; Szymanski, P.; Loh, J. Y. Y.; Kherani, N. P.; El-Sayed, M. A.; Ozin, G. A.; Singh, C. V. Photoexcited Surface Frustrated Lewis Pairs for Heterogeneous Photocatalytic CO2 Reduction. *J. Am. Chem. Soc.* **2016**, *138*, 1206−1214.
(177) Huš, M.; Kopač, D.; Likozar, B. Catalytic Hydrogenation of Carbon Dioxide to Methanol: Synergistic Effect of Bifunctional Cu/Perovskite Catalysts. *ACS Catal.* **2019**, *9*, 105−116.
(178) Kopač, D.; Likozar, B.; Huš, M. Catalysis of Material Surface Defects: Multiscale Modeling of Methanol Synthesis by CO2 Reduction on Copper. *Appl. Surf. Sci.* **2019**, *497*, 143783.
(179) Hammerschmidt, M.; Döpking, S.; Burger, S.; Matera, S. Field Heterogeneities and Their Impact on Photocatalysis: Combining Optical and Kinetic Monte Carlo Simulations on the Nanoscale. *J. Phys. Chem. C* **2020**, *124*, 3177−3187.
(180) Chueh, W. C.; Falter, C.; Abbott, M.; Scipio, D.; Furler, P.; Haile, S. M.; Steinfeld, A. High-Flux Solar-Driven Thermochemical Dissociation of CO 2 and H 2 O Using Ceria Using g the Sun to Make Fuels. *Science (Washington, DC, U. S.)* **2010**, *330*, 1797−1801.
(181) Matera, S.; Maestri, M.; Cuoci, A.; Reuter, K. Predictive-Quality Surface Reaction Chemistry in Real Reactor Models Integrating First-Principles Kinetic Monte Carlo Simulations Inot Computational Fluid Dynamics. *ACS Catal.* **2014**, *4*, 4081−4092.
(182) Matera, S.; Blomberg, S.; Hoffmann, M. J.; Zetterberg, J.; Gustafson, J.; Lundgren, E.; Reuter, K. Evidence for the Active Phase of Heterogeneous Catalysts through In Situ Reaction Product Imaging and Multiscale Modeling. *ACS Catal.* **2015**, *5*, 4514−4518.
(183) Braham, R. J.; Harris, A. T. A Complete Multi-Scale Simulation of Light Absorption within a Fluidized Bed Photoreactor Using Integrated Particle, Fluid and Photon Behaviour Models. *Phys. Chem. Chem. Phys.* **2013**, *15*, 12373−12385.
(184) Chu, F.; Li, S.; Chen, H.; Yang, L.; Ola, O.; Maroto-Valer, M.; Du, X.; Yang, Y. Modeling Photocatalytic Conversion of Carbon Dioxide in Bubbling Twin Reactor. *Energy Convers. Manage.* **2017**, *149*, 514−525.
(185) Zhang, H.; Smith, J. D. Investigating Influences of Geometric Factors on a Solar Thermochemical Reactor for Two-Step Carbon Dioxide Splitting via CFD Models. *Sol. Energy* **2019**, *188*, 935−950.
(186) Bhatta, S.; Nagassou, D.; Mohsenian, S.; Trelles, J. P. Photo-Thermochemical Decomposition of Carbon-Dioxide in a Direct Solar Receiver-Reactor. *Sol. Energy* **2019**, *178*, 201−214.
(187) Du, C.; Wang, X.; Chen, W.; Feng, S.; Wen, J.; Wu, Y. A. CO2 Transformation to Multicarbon Products by Photocatalysis and Electrocatalysis. *Mater. Today Adv.* **2020**, *6*, 100071.
(188) Choi, Y.; Liu, P. Understanding of Ethanol Decomposition on Rh(1 1 1) from Density Functional Theory and Kinetic Monte Carlo Simulations. *Catal. Today* **2011**, *165*, 64−70.
(189) Prats, H.; Álvarez, L.; Illas, F.; Sayós, R. Kinetic Monte Carlo Simulations of the Water Gas Shift Reaction on Cu(1 1 1) from Density Functional Theory Based Calculations. *J. Catal.* **2016**, *333*, 217−226.
(190) Sutton, J. E.; Panagiotopoulou, P.; Verykios, X. E.; Vlachos, D. G. Combined DFT, Microkinetic, and Experimental Study of Ethanol Steam Reforming on Pt. *J. Phys. Chem. C* **2013**, *117*, 4691−4706.
(191) Novell-Leruth, G.; Ricart, J. M.; Pérez-Ramírez, J. Pt(100)-Catalyzed Ammonia Oxidation Studied by DFT: Mechanism and Microkinetics. *J. Phys. Chem. C* **2008**, *112*, 13554−13562.
(192) Schaefer, C.; Jansen, A. P. J. Coupling of Kinetic Monte Carlo Simulations of Surface Reactions to Transport in a Fluid for

https://dx.doi.org/10.1021/acscatal.0c02557
ACS Catal. 2020, 10, 14984−15007

Heterogeneous Catalytic Reactor Modeling. *J. Chem. Phys.* **2013**, *138*, 054102.

https://dx.doi.org/10.1021/acscatal.0c02557
ACS Catal. 2020, 10, 14984−15007